Development of a Cellulose Nanocrystal–Paper Composite as a Substrate to Fabricate Robust Electroconductive Circuits

July 2020

林　冠萱

Development of a Cellulose Nanocrystal–Paper Composite as a Substrate to Fabricate Robust Electroconductive Circuits

A Dissertation Submitted to
the Graduate School of Life and Environmental Sciences,
the University of Tsukuba
in Partial Fulfillment of the Requirements
for the Degree of Doctor of Philosophy in Bioresource Engineering
(Doctoral Program in Appropriate Technology and Sciences for Sustainable Development)

林　冠萱

Content

Content ---- I
Figure Captions ---- III
Table Captions ---- V
Acknowledgement ---- VI
Abbreviation and symbol ---- VII
Abstract ---- XI
Chapter 1 General Introduction ---- 1
1.1 Motivation ---- 1
1.2 Objective ---- 2
1.3 Printed electronic device ---- 2
1.4 Cellulose-based substrate ---- 3
Reference ---- 6
Chapter 2 Surface Charge of Cellulose Nanocrystals and its Characterizations ---- 9
2.1 Abstract ---- 9
2.2 Introduction ---- 9
2.3 Experimental ---- 13
2.3.1 Material ---- 13
2.3.2 CNC preparation ---- 13
2.3.3 Dimensional measurement ---- 16
2.3.4 Elemental analysis ---- 16
2.3.5 Surface chemistry information ---- 16
2.3.6 Potentiometric titration ---- 17
2.3.7 Zeta potential calculation ---- 17
2.3.8 Zeta potential and electrophoretic mobility measurement ---- 18
2.4 Result and discussion ---- 19
2.4.1 Dimensional information of dried CNCs ---- 19
2.4.2 Surface morphology ---- 22
2.4.3 Charging behavior and surface environment of C-CNCs ---- 29
2.4.4 Analysis of electrophoretic mobility of C-CNCs ---- 32
2.5 Conclusion ---- 38
Reference ---- 39
Chapter 3 Development of Robust Conductive Tracks by Undercoating Cellulose Nanocrystal-formulated Ink ---- 42

3.1 Abstract ---- 42
3.2 Introduction ---- 42
3.3 Experimental ---- 44
3.3.1 Sample preparation ---- 44
3.3.2 CNC properties ---- 44
3.3.3 Ink-wettability of CNC pre-printed samples ---- 45
3.3.4 Topographical observation of CNC pre-printed samples ---- 45
3.3.5 Surface appearance ---- 45
3.3.6 Evaluation of the improved W-AgNP area ---- 45
3.4 Result and discussion ---- 46
3.4.1 Ink-wettability of samples ---- 46
3.4.2 Roughness evaluation ---- 46
3.4.3 Interaction between a silver track and printed CNCs ---- 46
3.4.4 Electrical performance of printed silver area ---- 50
3.4.5 Surface appearance ---- 54
3.5 Conclusion ---- 61
Reference ---- 62
Chapter 4 Fabrication of Cellulose Nanocrystal-based Transparent Conductive Device ---- 63
4.1 Abstract ---- 63
4.2 Introduction ---- 63
4.3 Experimental ---- 65
4.3.1 Sample preparation ---- 65
4.3.2 Characterization of films ---- 66
4.3.3 Structure of films and oil-based conductive tracks ---- 66
4.4 Result and discussion ---- 71
4.4.1 Characterization of films ---- 71
4.4.2 Mechanical property and wettability of films ---- 76
4.4.3 Topographical observation of films and O-AgNP areas ---- 79
4.4.4 Electrical performance of O-AgNP tracks ---- 83
4.5 Conclusion ---- 85
Reference ---- 86
Chapter 5 Overall Conclusion ---- 87

Figure Captions

Figure 1 Transmission electron micrograph of C-CNCs. 20
Figure 2 TEM observation of P-CNCs prepared with different sulfuric acid concentrations: (a) 63%; (b) 46%. 21
Figure 3 Detection of S and Na in "SA6345-2PN". 24
Figure 4 FT-IR spectra of C-CNCs and some of P-CNCs. 26
Figure 5 XPS spectrum and magnification of S2p3/2. 27
Figure 6 XPS spectrum of O1s in "SA6345-2PN" and C-CNCs..... 28
Figure 7 Surface charge density of C-CNCs..... 30
Figure 8 Fitting of theoretical equations when the surface charge density and distance between the particle surface and slipping plane are assumed to be -0.107 C/m^2 and 0.65 nm, respectively. 34
Figure 9 Fitting of theoretical equations including the Ohshima-Overbeek (length) equation as the best fitted approximation. 35
Figure 10 An effect of the CNCs length depicted with "Ohshima-Overbeek (length) eq." with an assumption that the radius, zeta potential, and surface charge density are constant (independent with the length of CNCs). 37
Figure 11 Side view of printed samples. 47
Figure 12 Schematic of SEM samples without CNCs (a) and with CNCs (b). 48
Figure 13 Schematic of how to subject W-AgNP-printed surface to friction. 49
Figure 14 Contact angles of W-AgNPs ink on photo-grade inkjet paper with no CNCs (No CNC), 1 layer (C1), 5 layer (C5), 10 layer (C10), and 15 layer (C15) CNCs printed. 51
Figure 15 Roughness values of samples with a scanned area of a 10 μm square. ... 52
Figure 16 Area ratio of silver nanoparticle layer remaining after frictions. 53
Figure 17 Resistance of silver layers before (left) and after friction (right). 55
Figure 18 Surface structure of the three areas: (a) paper surface, (b) printed CNCs, and (c) printed W-AgNPs. 56
Figure 19 Cross section of CNC-unprinted/printed area. 57
Figure 20 Cross section between CNC-printed area (C1)/AgC1: (a) whole view and (b) close-up of the red rectangle in (a) with strap-shaped structures denoted by arrows. 58
Figure 21 Penetration of W-AgNP ink on different layers of CNC undercoats..... 59
Figure 22 Silver without printed CNCs: (a) damage caused by cutting, (b) Silver layer peeled off, and (c) inkjet paper surface after the silver layer peeled off. 60
Figure 23 ZS tensile strength measurement. 69

Figure 24 Observation of cross section by FIB-SEM. First, a brick of platinum was coated, as the arrows point in (a) and (b), in front of an ideal place where circled by the broken line in (a). Then, the hole as (b) was dug by an ion beam. 70
Figure 25 Fabricated C-films and CF-films. (b): Transparent C-film (Take "C-40" as example). (c): Transparent CF-film (Take "CF3-40" as example). 72
Figure 26 Cross section view of a C-film. 73
Figure 27 A C-film (a, b) and CF-film (c, d) were put between cross polarizers. In (a) and (c), the left side is the place without films inside but "C-40" and "CF9-40" was put in the right side of (a) and (c) respectively. Then, (b) and (d) are close-ups of the red rectangles in (a) and (c), respectively. 74
Figure 28 CF-films were put between cross polarizers: from (a) to (j) are CF-0-40, CF-1-40, CF-2-40, CF-3-40, CF-4-40, CF-5-40, CF-6-40, CF-7-40, CF-8-40, CF-9-40. The left side in each photo is the place without films inside. . 75
Figure 29 (a): ZS tensile strength and grammage of films. (b): ZS tensile strength and CNF ratio of films. 77
Figure 30 Folding endurance and CNF ratio. 78
Figure 31 (a): Surface of a C-film ("C-40" as an example). (b): Surface of "CF-0-40". 80
Figure 32 Ground of O-AgNPs on a film ("C-40" as an example). 81
Figure 33 Thickness of an O-AgNP layer on (a) "C-40", (b) "CF10-40", and (c) "CF9-40". 82
Figure 34 Design of the circuit on a film. 84

Table Captions

Table 1 Hydrolysis conditions and sample names in P-CNCs. 15
Table 2 Summary of hydrolysis conditions and the resulted properties. 23
Table 3 Elemental composition of C-CNCs. 31
Table 4 List of C-films and CF-films. 68

Acknowledgement

I appreciate everyone who have accompanied me these years in Japan. It is not expected before studying here though, I appreciate the turning point in my life to bring me here.

First of all, I would like to express my very great appreciation to my advisor, professor Enomae, who encouraged me always. Advice given by committee members, Prof. Akiko Nakagawa-Izumi, Prof. Feng-Cheng Chang, and Prof. Motoyoshi Kobayashi, have been a great help. My grateful thanks are also extended to all lab members: Ms. Shimazaki for helping me a lot with complicated paper works; Dr. Xu, Dr. Halim, and Mr. Hu for helping me come up with ideas for experiments; Takeuchi for helping me every time when I met problems with Japanese; each one for bringing me happiness every day. Also, I thank members belonging to another lab and open facility, Dr. Hirose, Dr. Sugimoto, Dr. Tanigawa, Ms. Tawara, Ms. Tetsuka, Mr. Ueda, who taught me the operation of equipment, code writing, and gave me comments.

Secondly, I appreciate University of Tsukuba, for not only providing a best experimental environment but also Japanese courses. I wish to thank people for their help; my Japanese teachers who helped me improving the language skills; my friends and my previous lab in Taiwan for helping me build up background skills and accompanying with me to overcome obstacles; of course, my friends in Japan, for broadening my horizons and staying with me always.

Finally, I wish to thank my dear family, especially my parents for bringing me to such a wonderful world and the one who will enjoy life and grow old together hand in hand. I appreciate God's blessings to accomplish my study in this year. Though, this year, 2020, seems to be a tough year, it is my honor to stay safe and health at the present, and I hope all will be well soon.

Abbreviation and symbol

Abbreviation	Description
AgNPs	silver nanoparticles
AgC1, AgC5, AgC10, AgC15	printed mono-layer W-AgNPs ink on 1 to 15 layers of CNCs
C1, C5, C10, C15	printed 1, 5, 10, and 15 layers of CNCs
CNCs	cellulose nanocrystals
CNFs	cellulose nanofibers
CNTs	carbon nanotubes
Cr.I.	crystallinity index
C-CNCs	commercially available CNCs
C-films	films made by CNCs; sample list is in Table 4
CF-films	Films made by CNCs and CNFs; sample list is in Table 4
DD water	double-distilled water
DFM	dynamic force mode
DOD	drop on demand
EPMA	electron probe micro analyzer
FE-SEM	field emission scanning electron microscopy
FT-IR	diffuse reflectance infrared Fourier transform spectroscopy
FIB-SEM	focused ion beam-scanning electron microscopy
LED	light-emitting diode

O-AgNPs ink	oil-based silver nanopaste
PANI	polyaniline
PB	Poisson-Boltzmann
PEDOT:PSS	poly(ethylene-dioxythiophene):poly(styrene sulfonate
PET	polyethylene terephthalate
P-CNCs	CNCs extracted from wood pulp; sample list is in Table 1
p-DADMAC	poly(diallyldimethyl-ammoniumchloride)
RFID	radio-frequency identification
RH	relative humidity
SPM	scanning probe microscope
TEM	transmission electron microscopy
TEMPO	2,2,6,6-tetra-methylpiperidine-1-oxyl
TEMPO-CNCs	TEMPO-oxidized CNCs
TEMPO-CNFs	TEMPO-oxidized cellulose nanofibers
W-AgNPs ink	water-based silver nanoparticles ink
XPS	x-ray photoelectron spectroscopy
ZS	zero-span

Symbol	Description
a	particle radius
c	concentration of 1-1 electrolyte
D	width
e	elementary charge
k_B	Boltzmann constant
$K_n(x)$	modified Bessel function of the second kind of order n
L	length
$m\pm$	dimensionless ionic drag coefficient
N_A	Avogadro number
T	absolute temperature
Z	valence of counterions
Ψ_s	surface potential
ε_0	dielectric constants of vacuum
ε_r	dielectric constants of water
η	viscosity
κ	Debye–Hückel parameter
μ	electrophoretic mobility
$\mu_{measured}$	measured electrophoretic mobility
$\mu_{theoretical}$	calculated electrophoretic mobility
μ_{smol}	electrophoretic mobility calculated by Smoluchowski's equation

$\mu_{\perp}^{OO}$	electrophoretic mobility calculated by Ohshima-Overbeek (Perpendicular) equation
μ_{av}^{OO}	electrophoretic mobility calculated by Ohshima-Overbeek (averaged) equation
$\mu_{av}^{OO(L)}$	electrophoretic mobility calculated by Ohshima-Overbeek (length) equation
ζ	zeta potential
$\zeta_{theoretical}$	zeta potential estimated by solving the PB equation as an electric potential at the slipping plane in an electrical double layer
σ	surface charge density
X_s	the distance from the surface of a cylinder to an assumed slipping plane

Abstract

Cellulosic-based materials were chosen as a substrate for an electro-conductive device because of environmental friendliness. Then, inkjet printing, as a well-known technology, was applied to introduce conductive ink onto substrates. In Chapter 2, cellulose nanocrystals (CNCs) were characterized for further applications as either an undercoat of paper or main component for transparent film fabrications. The formation of sulfate groups, which provide negative charge on CNC surfaces, was studied in controlled acid hydrolysis conditions. This thesis examined whether such strong negative charge can be a reason for the unique colloidal property and resulting in a well-dispersed CNC suspension in water. In Chapter 3, CNCs were applied as an undercoat on a photo-grade inkjet paper to improve the continuity and robustness of conductive tracks on it. In Chapter 4, the particle surface environment of CNCs was presumed to exhibit liquid crystal behavior, forming a film with a helical structure which showed a birefringent pattern by cross polarization. Then, transparent CNC films were fabricated to be heat-resistant and conductive tracks on the film had a really low resistance after sintering it.

Chapter 1

General Introduction

1.1 Motivation

Nowadays, electric devices occur everywhere in daily life, such as antennas, transistors, displays, capacitors, solar cells, and so on. With a high speed of technological improvement, the penetration of electric products also has become rapid; for example, radio-frequency identification (RFID) tags were produced by printing and used in fashion industry. [1] However, a challenge to end-of-life disposal problems and environmental concerns is unignorable. Paper is potentially appropriate to deal with this tough situation and regarded as an optimal material to design and fabricate conductive substrates. Sustainable electronics based on paper have been drawing strong interest especially due to its material flexibility and low prices. Besides, a transparent device is attractive in opto-electronics though usually there is a trade-off between transparency and conductivity. Cellulose–the main component of a paper– provides paper with transparency by control of its nanoscale structure in designing the demanded paper properties.[2–5] Hence, both conventional paper and novel transparent papers were intended to be taken into consideration in this study to be an excellent substrate for electroconductive materials. Subsequently, considering that the printing industry commonly uses paper products, this technique, if established, is expected to fabricate flexible, cost-effective, environmentally-friendly electronic products with necessary circuits on it. Also, printed electronics has been tried with a flexible substrate to improve flexible electronics for decades.[3, 6–9] However, it was reported that the usage of nanocellulose as a substrate for printed electronics was still limited.[8] Thus, this

study focused on the development of a flexible paper- or nanocellulose-based substrate for electroconductive component fabricated by printing.

1.2 Objective

The aim of this study is to fabricate cellulose-based conductive devices. In Chapter 2, the colloidal surface properties of cellulose nanocrystals (CNCs) as a form of suspended particles were regarded as an important key factor for uniform dispersion in an aqueous suspension. In this view, as a homogeneous CNC suspension is known to exhibit liquid crystal behavior, the birefringence was examined. In Chapter 3, CNCs were printed initially on a paper substrate as an undercoat to improve electroconductivity of silver tracks fabricated on it by printing an aqueous silver nanoparticles (AgNPs) ink. The undercoat successfully functioned also as a reinforcement to create robust tracks. Furthermore, in Chapter 4, CNCs and cellulose nanofibers (CNFs) mixture were used to form transparent films. The unique properties owing to self-assembly arrangement induced by their surface charge was observed, and then the films were tested to examine if it was possible to create electroconductive devices from a conductive AgNPs ink on this substrate.

1.3 Printed electronic device

In this study, piezoelectric “drop on demand” (DOD) technology is used for an inkjet printer. Print heads with 16 nozzles are driven by a piezoelectric actuator, releasing ink droplets when forced by applied voltage. Also, this non-contact process brings a possibility of depositing a thin layer at a high printing speed at relatively high resolution. A two-stage process involving ink sorption and ink transparentization was reported to be influenced by the substrate surface properties. [10]

To create printed electronic devices, the selection of electrically functional components for ink is the first mission. Conductive polymers such as poly(ethylene-

dioxythiophene):poly(styrene sulfonate) (PEDOT:PSS), polypyrrole, poly(p-phenylene ethynylene), and polyaniline (PANI) were reported to be able to print or coat on cellulosic substrates as inks. [11–14] Besides, carbon-based particles like graphene oxide and carbon nanotubes (CNTs) were tried. [15–18] Though conductive polymers and carbon-based particles possess a moderate conductivity, they are reported to exhibit transparency and flexibility and thus became an interesting choice of screens. [19] Moreover, the high intrinsic electrical mobility and high mechanical strength, as well as the high transparency, are characteristic of graphene and CNTs, and beneficial for the low-cost printed electronics development.

Metallic inks made from silver, gold, and copper have been popular in providing opaque tracks with a conductivity hundred times higher than conductive polymers and carbon-based particles. [7, 9, 10, 14, 20–23] After sintering, an interconnected phase among metallic particles is formed, resulting in a high conductivity. Although metallic inks are preferred in terms of conductivity, annealing is a required process which is also a challenge faced by the substrate.

1.4 Cellulose-based substrate

As is well known, paper is attractive in terms of flexibility, cost, and environmental friendliness in the inkjet printing industry. For a longtime, people have printed various information on paper. Nevertheless, paper has been used as a substrate for pigment and ink deposition, it is still a challenge to apply paper as a substrate of conductive inks. The porous structure, roughness, and complicated surface chemistry of paper lead to difficulties with functional applications like printed electronics. Ihalainen *et al*. [9] mentioned that reduced roughness led to a lower resistivity, whereas Hrehorova *et al*. [24] reported that after calendering, a decreased surface roughness decreased conductivity. Though a lower surface roughness brought advantages to improve

conductivity [9], a higher roughness at high frequencies might also improve conductivity by increasing ink anchoring.

Though it is still difficult to tell the proper "roughness scales" effect on conductivity [6], the dimension of fillers or fibers were suggested. [9, 25] In addition, lamination of a plastic layer or surface coating was reported to enhance the advantages of a paper substrate by adjusting porosity, roughness or improving moisture barrier properties. [6, 9] Polyethylene terephthalate (PET) is usually coated on paper to realize an optimal surface property. However, it is reported to be incomparable to CNF-based films, which are more compatible with epoxy coating or acrylic resin matrix. [26, 27]

Other than the proper porosity and roughness, an important factor influencing ink penetration and ink-film continuity is the interaction between ink and constituents of paper. Excessive interactions were reported to result in the agglomeration of ink and ununiform distribution of the ink. [28] According to the combination of ink and substrate, ink fixation agents were chosen as well. Poly(diallyldimethyl-ammoniumchloride) (p-DADMAC) was applied with PEDOT:PSS ink; however, it was reported to result in a decreased conductivity due to the cationic property of p-DADMAC. [29] TEMPO (2,2,6,6-tetra-methylpiperidine-1-oxyl)-oxidized CNCs (TEMPO-CNCs) were also tried as a coating on paper. Even though a TEMPO-CNCs coating increased roughness, ink anchoring was improved. [26] Then, as mentioned in the last part of section 1.3, metallic inks provide the highest conductivity by sintering. In this case, the substrate must withstand high temperature.

In an overall consideration, beside paper, CNCs and CNFs were focused in this study. With hydroxyl groups, intra- and inter-molecular hydrogen bonds are formed. Thanks to the hydrogen bonds, cellulose chains are arranged in a highly ordered crystalline region, whereas the remaining disordered structure is called an amorphous region. The extracted crystalline regions comprised of nano-scale cellulose is called

CNCs. Cellulose materials with nanometer-scales in width and a large aspect ratio are called CNFs. Both CNCs and CNFs have recently gained attention owing to the potential to serve as a functional reinforcement material, providing enhanced thermal, mechanical, optical, and gas-barrier properties, as a result of their highly ordered nanostructure. [30] However, when cellulose chains are broken down to nanoscale by either a chemical method or a mechanical method, not only amorphous regions decrease but also crystalline regions decrease to a certain degree. In other words, small-sized products undergo more reduction in the crystallinity. Thus, the key point is to maintain the crystallinity in CNCs preparation even during the reduction in size of cellulose.

The crystallinity was reported to be dependent on the source. Bacterial and tunicate CNCs provide a higher crystalline fraction than wood CNCs, or the CNCs from pure cellulose provided a crystallinity index (*Cr.I.*) higher than those prepared from wastepaper. [31, 32] However, the pretreatment of cellulose materials before acid hydrolysis such as alkali extraction and bleaching also played a role to change *Cr.I.*. [33] Thus, with a careful proper pretreatment, even a by-product of kraft pulping was proven to reach high crystallinity as CNCs. [34] Besides crystallinity, the cellulose source was also reported to affect the CNC length. Wastepaper or a softwood pulp was treated with a sulfuric acid hydrolysis process, and the products with a length of approximately 200 nm were obtained. [35–37] Then, sulfuric acid hydrolysis is a common way to extract CNCs with grafted negatively-charged sulfate group. With sulfate groups, CNCs induce electric repulsion between each other in an aqueous system; moreover, they exhibit self-assembly arrangement at a certain concentration, inducing liquid crystal behavior.

Reference

1 Yasuaki Yokoyama, WWD JAPAN.com, January 20, 2020, https://www.wwdjapan.com/articles/1012983 (last accessed on May 9, 2020).

2 Lagerwall, J.P.F.; Schütz, C.; Salajkova, M.; Noh, J-H.; Park, J.H.; Scalia, G.; Bergström L. Cellulose nanocrystal-based materials: from liquid crystal self-assembly and glass formation to multifunctional thin films. *NPG Asia Mater* **2014**, *6*, e80. https://doi.org/10.1038/am.2013.69

3 Koga, H.; Saito, T.; Kitaoka, T.; Nogi, M.; Suganuma, K.; Isogai, A. Transparent, conductive, and printable composites consisting of tempo-oxidized nanocellulose and carbon nanotube. *Biomacromolecules* **2013**, *14* (4), 1160–1165.

4 Majoinen, J.; Kontturi, E.; Ikkala, O.; Gray, D.G. SEM imaging of chiral nematic films cast from cellulose nanocrystal suspensions. *Cellulose* **2012**, *19*, 1599–1605.

5 Pan, J.; Hamad, W.; Straus S.K. Parameters affecting the chiral nematic phase of nanocrystalline cellulose films. *Macromolecules* **2010**, *43* (8), 3851–3858.

6 Agate, S.; Joyce, M.; Lucia, L.; Pal, L. Cellulose and nanocellulose-based flexible-hybrid printed electronics and conductive composites - A review. *Carbohydrate Polymers* **2018**, *198*, 249–260.

7 Hoeng, F.; Bras, J.; Gicquel, E.; Krosnicki, G.; Denneulin, A. Inkjet printing of nanocellulose–silver ink onto nanocellulose coated cardboard. *RSC Advances* **2017**, *7*, 15372–15381.

8 Hoeng, F.; Denneulinacd A.; Bras, J. Use of nanocellulose in printed electronics: a review. *Nanoscale* **2016**, *8*, 13131–13154.

9 Ihalainen, P.; Määttänen, A.; Järnström, J.; Tobjörk, D.; Österbacka, R.; Peltonen, J. Influence of surface properties of coated papers on printed electronics. *Industrial & Engineering Chemistry Research* **2012**, *51* (17), 6025–6036.

10 Zhang, Y.P.; Chodavarapu, V.P.; Kirk, A.G.; Andrews, M.P. Structured color humidity indicator from reversible pitch tuning in self-assembled nanocrystalline cellulose films. *Sensors and Actuators B: Chemical* **2013**, *176*, 692–697.

11 Sico, G.; Montanino, M.; De Girolamo Del Mauro, A.; Imparato, A.; Nobile, G.; Minarini, C. Effects of the ink concentration on multi-layer gravure-printed PEDOT:PSS. *Organic Electronics* **2015**, *28*, 257–262.

12 Valtakari, D.; Liu, J.; Kumar, V.; Xu, C.; Toivakka, M.; Saarinen, J.J. Conductivity of PEDOT:PSS on spin-coated and drop cast nanofibrillar cellulose thin films. *Nanoscale Res Lett* **2015**, *10*. https://doi.org/10.1186/s11671-015-1093-y

13 McCarthy, J.E.; Hanley, C.A.; Brennan, L.J.; Lambertinib, V.G.; Gun'ko, Y.K. Fabrication of highly transparent and conducting PEDOT:PSS films using a formic acid treatment. *Journal of Materials Chemistry C* **2014**, *2*, 764–770.

14 Mandal, S.; Purohit, G.; Katiyar, M. Inkjet printed organic thin film transistors: achievements and challenges. *Materials Science Forum* **2012**, *736*, 250–274.

15 Secor, E.B.; Prabhumirashi, P.L.; Puntambekar, K.; Geier, M.L.; Hersam, M.C. Inkjet printing of high conductivity, flexible graphene patterns. *The Journal of Physical Chemistry Letters* **2013**, *4* (8), 1347–1351.

16 Mirri, F.; Ma, A.W.K.; Hsu, T.T.; Behabtu, N.; Eichmann, S.L.; Young, C.C.; Tsentalovich, D.E.; Pasquali, M. High-performance carbon nanotube transparent conductive films by scalable dip coating. *ACS Nano* **2012**, *6* (11), 9737–9744.

17 Torrisi, F.; Hasan, T.; Wu, W.; Sun, Z.; Lombardo, A.; Kulmala, T.S.; Hsieh, G-W.; Jung, S.; Bonaccorso, F.; Paul, P.J.; Chu, D.; Ferrari, A.C. Inkjet-printed graphene electronics. *ACS Nano* **2012**, *6* (4), 2992–3006.

18 Huang, J.; Zhu, H.; Chen, Y.; Preston, C.; Rohrbach, K.; Cumings, J.; Hu, L. Highly transparent and flexiblenanopaper transistors. *ACS Nano* **2013**, *7* (3) 2106–2113.

19 Huang, L.; Huang, Y.; Liang, J.; Wan, X.; Chen, Y.; Graphene-based conducting inks for direct inkjet printing of flexible conductive patterns and their applications in electric circuits and chemical sensors. *Nano Research* **2011**, *4***,** 675–684.

20 Lee, S-H.; Cho, Y-J. Characterization of silver inkjet overlap-printing through cohesion and adhesion. *Journal of Electrical Engineering and Technology* **2012**, *7* (1), 91–96.

21 Tsai, C-Y.; Chang, W-C.; Chen, G-L.; Chung, C-H.; Liang, J-X.; Ma, W-Y.; Yang, T-N. A study of the preparation and properties of antioxidative copper inks with high electrical conductivity. *Nanoscale Research Letters* **2015**, *10*, 357.

22 Abhinav, K.V.; Rao R.V.K.; Karthik, P.S.; Singh, S.P. Copper conductive inks: synthesis and utilization in flexible electronics. *RSC Advances* **2015**, *5*, 63985–64030.

23 Larmagnac, A.; Eggenberger, S.; Janossy, H.; Voros, J. Stretchable electronics based on Ag-PDMS composites. *Scientific Reports* **2015**, *4,* 7254.

24 Hrehorova, E.; Wood, L.K.; Pekarovic, J.; Pekarovicova, A.; Fleming, P.D.; Bliznyuk, V. *The properties of conducting polymers and substrates for printed electronics.* **2005**.

25 Torvinen, K.; Sievänen, J.; Hjelt, T.; Hellén, E. Smooth and flexible filler-nanocellulose composite structure for printed electronics applications. *Cellulose* **2012**, *19*, 821–829.

26 Jung, Y.; Chang, T.; Zhang, H.; Yao, C.; Zheng, Q.; Yang, V.W.; Mi, H.; Kim, M.; Cho, S.J.; Park, D-W.; Jiang, H.; Lee, J.; Qiu, Y.; Zhou, W.; Cai, Z.; Gong, S.; Ma, Z. High-performance green flexible electronics based on biodegradable cellulose nanofibril paper. *Nature Communications* **2015**, *6,* 7170.

27 Okahisa, Y.; Yoshida, A.; Miyaguchi, S.; Yano, H. Optically transparent wood–cellulose nanocomposite as a base substrate for flexible organic light-emitting diode displays. *Composites Science and Technology* **2009**, *69* (11–12), 1958–1961.

28 Angelo, P.D.; Farnood, R.R.; Sodhi, R.N.; Cole, G.B. Conductivity of inkjet-printed PEDOT:PSS-SWCNTs on uncoated papers. *Nordic Pulp & Paper Research Journal* **2012**, *27* (2), 486–495.

29 Trnovec, B.; Stanel, M.; Hahn, U.; Hübler, A.C.; Kempa, H.; Sangl, R.; Forster, M. Coated paper for printed electronics. *Professional Papermaking* **2009**, *1*, 48–51.

30 Sehaqui, H.; Salajkova, M.; Zhou, Q.; Berglund, L.A. Mechanical performance tailoring of tough ultra-high porosity foams prepared from cellulose I nanofiber suspensions. *Soft Matter* **2010**, *6*, 1824–1832.

31 Sacui, I.A.; Nieuwendaal, R.C.; Burnett, D.J.; Stranick, S.J.; Jorfi, M.; Weder, C.; Foster, E.J.; Olsson, R.T.; Gilman, J.W. Comparison of the properties of cellulose nanocrystals and cellulose nanofibrils isolated from bacteria, tunicate, and wood processed using acid, enzymatic, mechanical, and oxidative methods. *Acs Appl. Mater. Interfaces* **2014**, *6*, 6127–6138.

32 Danial, W.H.; Majid, Z.A.; Muhid, M.N.M.; Triwahyono, S.; Bakar, M.B.; Ramli, Z. The reuse of wastepaper for the extraction of cellulose nanocrystals. *Carbohydr. Polym.* **2015**, *118*, 165–169.

33 Chieng, B.W.; Lee, S.H.; Ibrahim, N.A.; Then, Y.Y.; Loo, Y.Y. Isolation and characterization of cellulose nanocrystals from oil palm mesocarp fiber. *Polymers* **2017**, *9*, 355; doi: 10.3390/polym9080355.

34 Aguayo, M.G.; Pérez, A.F.; Reyes, G.; Oviedo, C.; Gacitúa, W.; Gonzalez, R.; Uyarte, O. Isolation and characterization of cellulose nanocrystals from rejected fibers originated in the kraft pulping process. *Polymers* **2018**, *10*, 1145.

35 Danial, W.H.; Majid, Z.A.; Muhid, M.N.M.; Triwahyono, S.; Bakar, M.B.; Ramli, Z. The reuse of wastepaper for the extraction of cellulose nanocrystals. *Carbohydr. Polym.* **2015**, *118*, 165–169.

36 Dong, X.M.; Revol, J.F.; Gray, D.G. Effect of microcrystallite preparation conditions on the formation of colloid crystals of cellulose. *Cellulose* **1998**, *5*, 19–32.

37 Abdul Khalil, H.; Davoudpour, Y.; Islam, M.N.; Mustapha, A.; Sudesh, K.; Dungani, R.; Jawaid, M. Production and modification of nanofibrillated cellulose using various mechanical process: A review. *Carbohydr. Polym.* **2014**, *99*, 649–665.

Chapter 2

Surface Charge of Cellulose Nanocrystals and its Characterizations

2.1 Abstract

An effect of surface charge of cellulose nanocrystals (CNCs) on their behavior in an aqueous system was investigated in this chapter. Sulfuric acid hydrolysis was applied for studying the graft of sulfate groups in various hydrolysis environments. Elemental analysis and composition were investigated; then, surface functional groups, assumed to be sulfate groups, were examined. After confirming the presence of sulfate groups which caused a negative-charged surface, the surface charge density was calculated based on potentiometric titration. Finally, colloidal behavior of CNCs was studied by focusing on the model-fitting of electrophoretic mobility. CNCs prepared via strong hydrolysis conditions such as a high sulfuric acid concentration or a high hydrolysis temperature suggested a more significant presence of sulfate groups than the others. Furthermore, the result of model-fitting pointed out an unignorable relaxation effect caused by the highly charged surface from sulfate groups.

2.2 Introduction

Cellulose is a sustainable bioresource and is abundant in nature. Because of the unique characteristics, CNCs with functional groups have recently gained considerable global attention in the field of materials science, particularly in exploring and applying such materials for industrial use. It was reported that, generally, higher acid concentrations would result in CNCs with higher surface charges and smaller sizes. Higher hydrolysis temperatures and longer hydrolysis durations would result in smaller

CNCs as well. [1–5] However, dried CNC powder is preferred because of its efficient delivery, preference for further analysis, and antibacterial and antifungal effects, though it has been reported to be difficult to re-disperse in water. [6] To obtain a better re-dispersibility, the counterion exchange for neutral monovalent cations was recommended. [7] Chemical hydrolysis, particularly acid hydrolysis, has been proven as an effective solution for generating highly pure CNCs. [1, 8–10] The review literature suggested that chemical groups introduced on CNCs were dependent on the type of acid. [8, 11–13] Phosphoric acid hydrolyzed samples showed a low surface charge. [8] Besides, hydrochloric acid hydrolyzed samples exhibited more intermolecular hydrogen bonding. [13]

Owing to the steric effect, the hydroxyl groups on cellulose chains exhibit different reactivity characteristics. With the numbering system of carbon atoms, the locations of hydroxyl groups are determined in an anhydroglucose unit of cellulose. Thus, hydroxyl groups on the surface of cellulose can react with various chemicals and become derivatives with designed functions. The hydroxyl group at the C6 position as a primary alcohol with only one alkyl group bonded, whereas the hydroxyl groups at the C2 and C3 positions act as a secondary alcohol with two alkyl groups bonded. The hydroxyl group at the C6 position was found to have a reactivity 10 times faster than that at the C2 and C3 positions. [14] This rapid reaction implies that the hydroxyl groups on the surface of cellulose can react with hydrolysis agents, becoming derivatives with designed functions.

Sulfate groups were grafted onto CNCs prepared via sulfuric acid hydrolysis at the C6 position. Rod-like CNC particles were well dispersed in an aqueous system due to repulsive electric double layer force. [15] Thus, the understanding of the surface potential (Ψ) due to the charge of sulfate groups on the surface and an electrical double layer surrounding a CNC particle has become important to evaluate the stability of CNC

suspensions. In addition, the ability to form chiral nematic ordered phase was influenced by the surface charge, which is dependent on the acid chosen for hydrolysis. [16]

Electric potential decreases with an increasing distance from the particle surface in an electric double layer. Zeta potential (ζ), defined as the potential at the slipping plane in an interfacial double layer, can be used to evaluate the level of dispersion in a colloidal suspension; this is usually calculated considering the present electrolytes, solvent and other suspended particles, and temperature, among other factors. Several equations have been formulated to obtain ζ from electrophoretic mobility (μ) because a value of μ can be easily obtained as the ratio of the velocity of particles to the applied electric field. For this purpose, Smoluchowski's equation (eqn (1)), which is suitable for large spherical particles with a low ζ, was widely used in previous studies. [17, 18]

$$\mu_{smol} = \frac{\varepsilon_r \varepsilon_0 \zeta}{\eta} \quad (1),$$

where η is the solvent viscosity, ε_0 and ε_r are the dielectric constants of vacuum and water, respectively, and ζ is the zeta potential. However, CNCs are nanoscale thin rod-like particles with a ζ of approximately -25 mV [18] or with a surface charge density of approximately -0.1 C/m^2 [19]. When the surface charge is high and the size is small, Smoluchowski's equation is no longer available because of retardation and relaxation effects.

To consider the high surface potential and the resulting relaxation effect of a cylinder, Ohshima (2015) derived equations with a consideration of the relaxation effect based on equations provided by van der Drift et al. (1979), which account for cases of high surface potential. [20, 21] With consideration of the valence of counterions (Z) and dimensionless ionic drag coefficient ($m\pm$), eqn (2) is the μ for a cylinder in the

perpendicular orientation with the relaxation of the double layer (named "Ohshima-Overbeek perpendicular equation"). The averaged μ, "Ohshima-Overbeek averaged equation", is represented by $\mu_{av}{}^{OO} = \frac{(\mu_{smol}+2\mu_{\perp}{}^{OO})}{3}$, according to Ohshima (2015). These equations are applicable to low to moderately high ζ (< 100 mV).

$$\mu_{\perp}{}^{OO} = \frac{\varepsilon_r\varepsilon_0\zeta}{2\eta}\left\{1+\frac{1}{\left[1+\frac{2.55}{\kappa a\{1+exp(-\kappa a)\}}\right]^2}\right\}-$$

$$\frac{2\varepsilon_r\varepsilon_0\zeta}{3\eta}\left(\frac{Ze\zeta}{k_BT}\right)^2\left[\frac{\kappa a(\kappa a+0.162)}{2\{(\kappa a)^3+9.94(\kappa a)^2+18.7(\kappa a)+0.147exp(-9.41\kappa a)\}}+\right.$$

$$\left.\left(\frac{m_++m_-}{2}\right)\frac{9\kappa a\{\kappa a+0.361exp(-0.475\kappa a)+0.0878\}}{8\{(\kappa a)^3+10.8(\kappa a)^2+18.2(\kappa a)+0.0633\}}\right] \quad (2)$$

The theories mentioned above consider different aspects of the properties of the particles such as cylindrical shape, surface potential, and the relaxation effect and thus are suitable for estimating the charging properties of CNC colloidal particles. In this equation, κ, the Debye–Hückel parameter is introduced. The Debye length—thickness of double layer—is defined as an inverse of the Debye–Hückel parameter (κ^{-1}). The theoretical relationship between κ^{-1} and the concentration of the added 1-1 electrolyte is defined as eqn (3) [22]

$$\kappa^{-1} = \sqrt{\frac{\varepsilon_r\varepsilon_0 k_BT}{2N_Ace^2}} \quad (3)\,,$$

where ε_0 and ε_r are the dielectric constants of water and vacuum, respectively, k_B is the Boltzmann constant, T is the absolute temperature, N_A is the Avogadro number, e is the elementary charge, and c is the concentration of 1-1 electrolyte. Therefore, the product of κ and the particle radius (a), κa, could be regarded as the ratio of the particle radius to the Debye length, which is related to the contribution of curvature due to the thin cylindrical shape and plays a critical role in colloidal systems.

In this study, sulfuric acid was chosen to produce products with a high aspect ratio and with a negatively charged surface so that the resulting CNCs were expected to disperse in an aqueous system due to electrostatic repulsion between the particles. [23–25] With the purpose to expand the possibilities in the pulp and paper-making industry, we intended to clarify and justify the factors of the preparation conditions in considering CNC properties with the raw material of wood pulp. Elemental analysis, structure analysis, as well as electrophoretic mobility theoretical equations fitting were conducted to study CNC in terms of the shape and surface charge.

2.3 Experimental

2.3.1 Material

CNCs extracted from wood pulp, referred-to "P-CNCs", were taken for studying the relationship between the resulting properties and the hydrolysis conditions. Commercially available CNCs, (C-CNCs; Freeze-dried, University of Maine, Orono, ME, USA) were analyzed and set as the reference standard for evaluation of laboratory-made P-CNCs.

The bleached, dry hardwood pulp applied here (provided by Chung Hwa Pulp Corporation, Taiwan) was a mixture of eucalyptus (*Eucalyptus* spp.) and bixa (*Bixa* spp.). The chemical composition of the applied dry hardwood pulp was mainly cellulose (85–89%) and hemicelluloses (8–10%) with small impurity levels of lignin (<1%), ash (<0.5%), and lipid (<0.5%). Sodium hydroxide (NaOH; Showa Chemical Co. Ltd., Japan) was used for pretreatment and neutralization after acid hydrolysis. Sulfuric acid (95–98%, *w*/*w*) (Scharlau, Barcelona, Spain) was prepared into various concentrations for hydrolysis. The water used for this purpose was double-distilled water (DD water).

2.3.2 CNC preparation

The bleached hardwood pulp was first to cut into strips, alkaline extraction was performed as a pretreatment for the dry hardwood pulps. Strips of pulp were treated

with 3% (*w*/*w*) NaOH at 50 °C for 2 h, which would remove fatty acids, residual lignin, hemicelluloses, resin, and other impurities. Simultaneously, the amorphous region would also swell so that it would improve the effectiveness of acid hydrolysis later.

Products gained from the first step were filtered by using an aspirator (A100-S, EYELA, Tokyo, Japan) and a glass filter. Then, the pulp was hydrolyzed in air in a variety of conditions, as shown in Table 1, including sulfuric acid at concentrations of 46% and 63% (*w*/*w*), hydrolysis temperatures of 45 and 65 °C, and hydrolysis durations of 0.5, 1, and 2 h. The weight ratio of hardwood pulp to acid solution was set to 1:20 (g/mL), and P-CNCs were obtained after acid hydrolysis. After hydrolysis, 300 mL of DD water was added to stop the reaction. Then, a third step was conducted to remove the free acid. The suspension was transferred to a 50 mL centrifuge tube and then centrifuged at 5000 rpm for 10 min at least 3 times.

Titration was then conducted with a 10% (*w*/*w*) NaOH solution to gain redispersible P-CNC suspensions before dialyzing against water through membranes with a cutoff molecular weight of 12,000–14,000 (Membrane Filtration Products Inc., Seguin, TX, USA). Freeze-drying was chosen in this study because it has been reported as a way to dry samples without forming significantly larger aggregates than those seen in air-drying or spray-drying. [26] Thus, P-CNC powders were obtained by freeze-drying (Kingmech Co. Ltd., Taipei, Taiwan) after ultrasonication for 20 min (Crest Ultrasonics Corporation, Ewing Township, NJ, USA).

Table 1 Hydrolysis conditions and sample names in P-CNCs.

Sample name	Concentration (*w*/*w*%)	Temperature (°C)	Duration (h)
SA4645-0.5PN	46	45	0.5
SA4645-1PN	46	45	1
SA4645-2PN	46	45	2
SA4665-0.5PN	46	65	0.5
SA4665-1PN	46	65	1
SA4665-2PN	46	65	2
SA6345-0.5PN	63	45	0.5
SA6345-1PN	63	45	1
SA6345-2PN	63	45	2
SA6365-0.5PN	63	65	0.5
SA6365-1PN	63	65	1
SA6365-2PN	63	65	2

2.3.3 Dimensional measurement

Two methods were applied for determining dimensional properties. Transmission electron microscopy (TEM) (JEM-1200 EXII, JEOL, Japan and H7650, Hitachi, Japan) was used to measure the dimension of CNCs after drying on a TEM grid. A hydrodynamic size distribution was measured based on the dynamic light scattering technique (Zetasizer Nano-ZS, Malvern Instruments, England). For TEM measurements, CNC suspensions at 0.1% (w/w) were dropped on 20 mesh carbon coated TEM copper grids for TEM observations at 60 kV in accelerating voltage. The particle dimensions were analyzed using *ImageJ (https://imagej.nih.gov/ij/index.html)* for at least 30 different particles. Only individual particles with clear edges were measured. The length and width were determined as the distance between the two ends of each particle along the length axis and distance between the edges across the axial center, respectively.

The Stokes-Einstein equation introduces a relationship between the hydrodynamic size and the diffusion coefficient by Brownian motion. Then, the particle size and hydrodynamic size distribution of CNC particles were determined from the diffusion coefficient of particles indicated by the rate of fluctuation of the signal intensity analyzed by autocorrelation built in the instrument.

2.3.4 Elemental analysis

Contents of N, C, S, and H were determined by elemental analysis (Elemental analyzer: elementar vario EL cube, Germany). CNCs were packed into a tin-capsule and incinerated at a higher temperature than 1000 °C in the presence of oxygen to obtain oxides of N, C, and S. Subsequently, the mass of the oxides was detected and converted to the composition.

2.3.5 Surface chemistry information

An electron probe micro analyzer (EPMA; JXA-8530F, JEOL, Tokyo, Japan) was applied to investigate the elemental composition at the surface of CNCs. Samples were

coated with carbon and measured at an accelerating voltage of 10 kV. On the other hand, diffuse reflectance infrared Fourier transform spectroscopy (FT-IR; FTS-40, BIO-RAD, Hercules, CA, USA) and x-ray photoelectron spectroscopy (XPS; JPS-9010TR, JEOL, Tokyo, Japan) were applied to detect the surface functional groups and chemical bonds of CNCs.

2.3.6 Potentiometric titration

The surface charge of CNCs was measured by potentiometric acid-base titration with a pH meter integrated with a burette (Easy pH, Mettler Toledo, USA). A blank solution was prepared by mixing 25 mL of 0.01 M NaCl with 10 mL of 0.01 M HCl. Then, a titration curve of the blank was constructed by using 0.01 M NaOH under a CO_2-free system with continuous stirring and bubbling argon gas. A CNC suspension at approximately 0.3% (w/w) with 0.01 M HCl was then added into the blank sample and titrated again. Titration curves of the blank and CNCs were plotted with pH values calibrated by Gran's plot. The surface charge density (σ) was calculated from the volumes of the titrant added to blank and the suspension of CNCs at the same pH, CNC density at 1.6 g/cm^3 [27], and the specific surface area.

2.3.7 Zeta potential calculation

If the surface charge density is constant irrespective of pH or electrolyte concentration as expected from sulfate groups on CNCs, one can evaluate the surface potential as a function of the electrolyte concentration by using the solution following the Poisson-Boltzmann (PB) equation. $\zeta_{theoretical}$ of CNCs in the 1-1 electrolyte solution was estimated by solving the PB equation as an electric potential at the slipping plane in an electrical double layer with the idea reported by Ohshima (1998). [28] The relationship between the surface charge density, σ, and the surface potential, ψ_s, is approximated as eqns (4-6):

$$\sigma = \frac{\varepsilon_r \varepsilon_0 \kappa k_B T}{e} 2 \sinh\left(\frac{y_s}{2}\right) \left[1 + \left(\frac{1}{\beta^2} - 1\right) \frac{1}{\cosh^2\left(\frac{y_s}{4}\right)}\right]^{\frac{1}{2}} (4)$$

$$y_s = \frac{e\psi_s}{k_B T} \quad (5)$$

$$\beta = \frac{K_0(\kappa a)}{K_1(\kappa a)} \quad (6),$$

where $K_n(x)$ is the modified Bessel function of the second kind of order n.

Then, when the distance from the surface of a cylinder to an assumed slipping plane is decided as X_s, $\psi(X_s)$ could be written as

$$\psi(X_s) = \frac{2k_B T}{e} \ln\left[\frac{(1+DC)\left(1+\frac{1-\beta}{1+\beta}DC\right)}{(1-DC)\left(1-\frac{1-\beta}{1+\beta}DC\right)}\right] \quad (7),$$

where

$$C = \frac{K_0[\kappa(a+X_S)]}{K_0(\kappa a)} \quad (8)$$

and

$$D = \frac{\tanh\left(\frac{y_s}{4}\right)(1+\beta)}{1+\left[1-(1-\beta^2)\tanh^2\left(\frac{y_s}{4}\right)\right]^{\frac{1}{2}}} \quad (9).$$

Thus, $\zeta_{theoretical}$ could be approximated as the surface potential located at X_s from the particle surface.

2.3.8 Zeta potential and electrophoretic mobility measurement

Charged particles can electrophoretically migrate in solution in an applied electric field. The migration velocity of particles under these conditions is measured by laser Doppler velocimetry. The measured electrophoretic mobility ($\mu_{measured}$) was then calculated from a ratio of the migration velocity to the electric field intensity, reflecting the surface potential of colloidal particles. ζ of CNCs under different conditions were calculated based on the $\mu_{measured}$ using theoretical equations such as Smoluchowski's theory (eqn (1)). Solid polarization was reported to significantly affect electrophoretic

mobility only when an applied electric field was strong and a dielectric permittivity ratio of particle to solution was large. [29] In this study, however, the applied electric field was weak, and the dielectric permittivity ratio was small. Thus, the solid polarization effect is negligible. Data of $\mu_{measured}$ were collected at 20 °C using a Zetasizer from 20 data points after 3 runs, and the conversion for ζ_{Smol} was based on Smoluchowski's theory.

2.4 Result and discussion

2.4.1 Dimensional information of dried CNCs

Figure 1 shows a TEM micrograph of C-CNCs with information about dimensions. Spindle-shaped particles captured in this TEM image were analyzed, and their average length (*L*) and width (*D*) were determined to be 168±3 nm and 13.5±0.5 nm, respectively. Based on this information, the aspect ratio of C-CNCs (*L/D*) was calculated to be approximately 12.4.

Then, in contrast to the width, a significant difference of length between P-CNCs was noticed. When the concentration of sulfuric acid was as low as 46% (w/w), the hydrolysis temperature and duration influenced the length of the observed P-CNCs, which might not achieve complete hydrolysis to small-crystallized particles. P-CNCs obtained from hydrolysis for 0.5 h were longer than those hydrolyzed for 2 h; they were shorter after being treated at 65 °C compared with those treated at 45 °C. P-CNCs prepared using a high sulfuric acid concentration (63%) were shorter in length than those obtained using a low concentration (46%). The preferred length of CNCs is shorter than 500 nm; therefore, a sulfuric acid concentration as high as 63% (*w*/*w*) was suggested for use in the P-CNC preparation procedure (Figure 2).

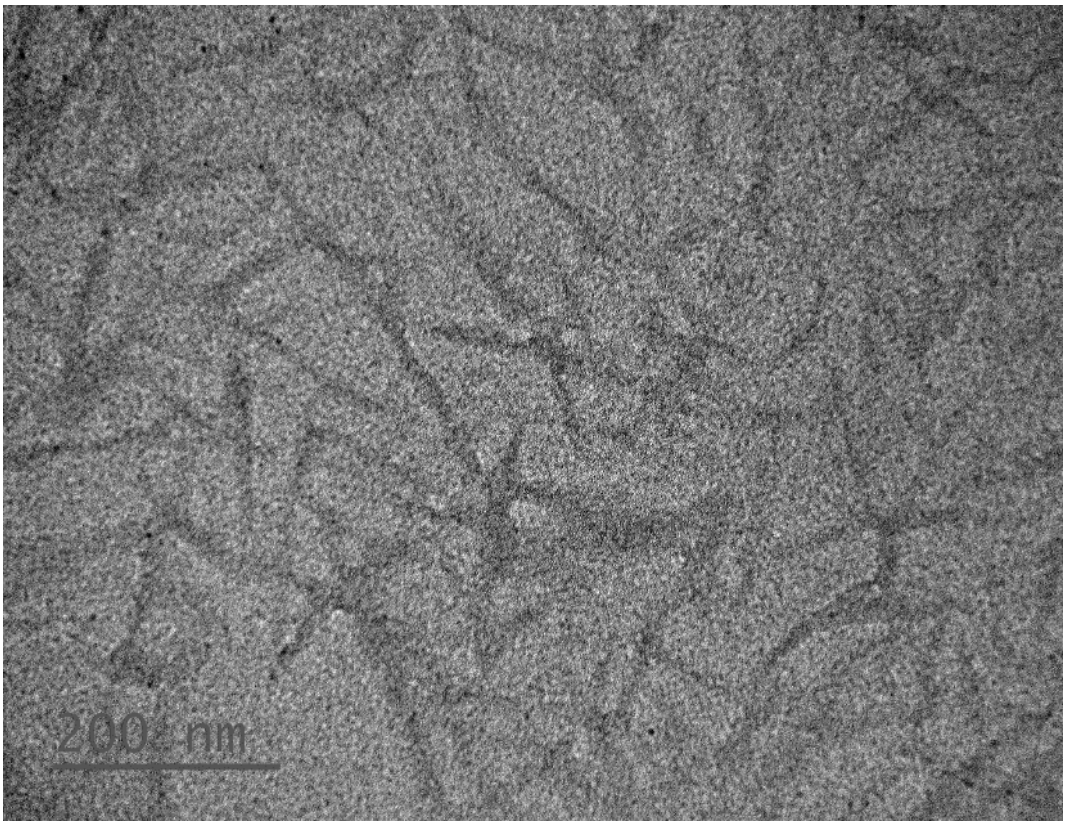

Figure 1 Transmission electron micrograph of C-CNCs.

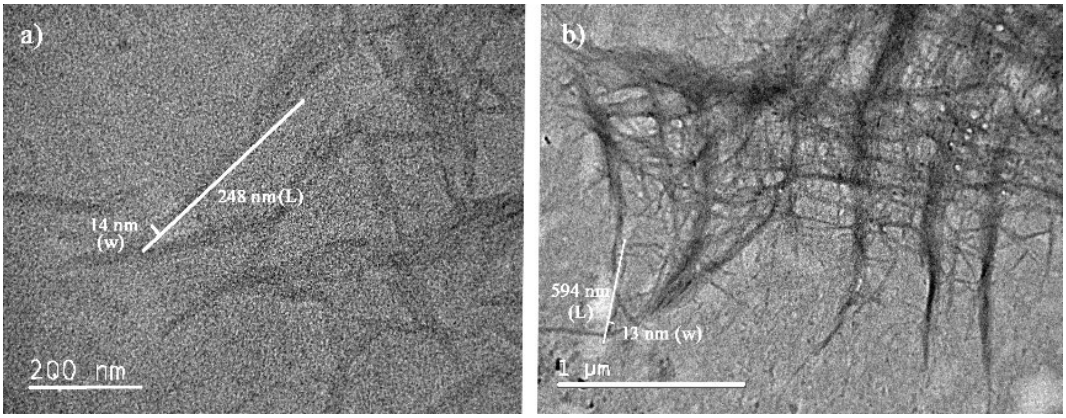

Figure 2 TEM observation of P-CNCs prepared with different sulfuric acid concentrations: (a) 63%; (b) 46%.

In summary, the resulting P-CNCs revealed an average length shorter than 500 nm for samples prepared at a high sulfuric acid concentration (63%, *w*/*w*). Similar conditions were also chosen in the literature, with the purpose of obtaining an ideal length.

2.4.2 Surface morphology

Commercial pulps are known to contain minerals because native ash and tap water washing are used. The mineral impurities might return to insoluble ash, though they should be dissolved during sulfuric acid hydrolysis. The minerals in the dry hardwood pulp contained magnesium, silicon, calcium, chlorine, and potassium, as shown in the resulting diagram from EPMA. Thus, careful pretreatment was deemed a necessary process, even though bleached pulp was chosen.

Silica, aluminum, and Magnesium were detected in hardwood pulp and in the sample prepared by 46% sulfuric acid, as suggested by EPMA results. Then, P-CNCs hydrolyzed with a 63% sulfuric acid at 45 °C for 2 h also had remaining magnesium and silicon residues (Figure 3), which meant they were removed by neither alkaline extraction nor hydrolysis at such a high sulfuric acid concentration. Less sulfate and sodium remained on the surface of P-CNCs hydrolyzed at 65 °C, as indicated by very weak peaks even under a high-resolution scan. Thus, a high temperature is not recommended for preparing re-dispersible P-CNCs. However, the P-CNCs hydrolyzed with 46% sulfuric acid showed the presence of other impurities such as calcium.

Table 2 Summary of hydrolysis conditions and the resulted properties.

Sample	Raw material	Sulfuric acid concentration (%, *w*/*w*)	Hydrolysis temp. (°C)	Hydrolysis duration (min)	Yield (%)	Length (nm)
C-CNCs	Wood pulp	--	--	--	--	168 ± 3
SA6345-2PN	Hardwood pulp	63	45	120	78	224 ± 23
SA6345-1PN	Hardwood pulp	63	45	60	79	229 ± 52
SA6345-0.5PN	Hardwood pulp	63	45	30	77	271 ± 42
SA6365-2PN	Hardwood pulp	63	65	120	51	210
SA4645-2PN	Hardwood pulp	46	45	120	82	472
Reid- AITF [23]	Softwood pulp	63	45	120	--	134 ± 56
Reid- Lab-made [23]	Cotton	64	45	45	--	132 ± 55
Beck-Candanedo- S2 [4]	Bleached softwood	64	45	45	--	120 ± 5
Beck-Candanedo- S1 [4]	Bleached softwood	64	45	25	--	141 ± 6

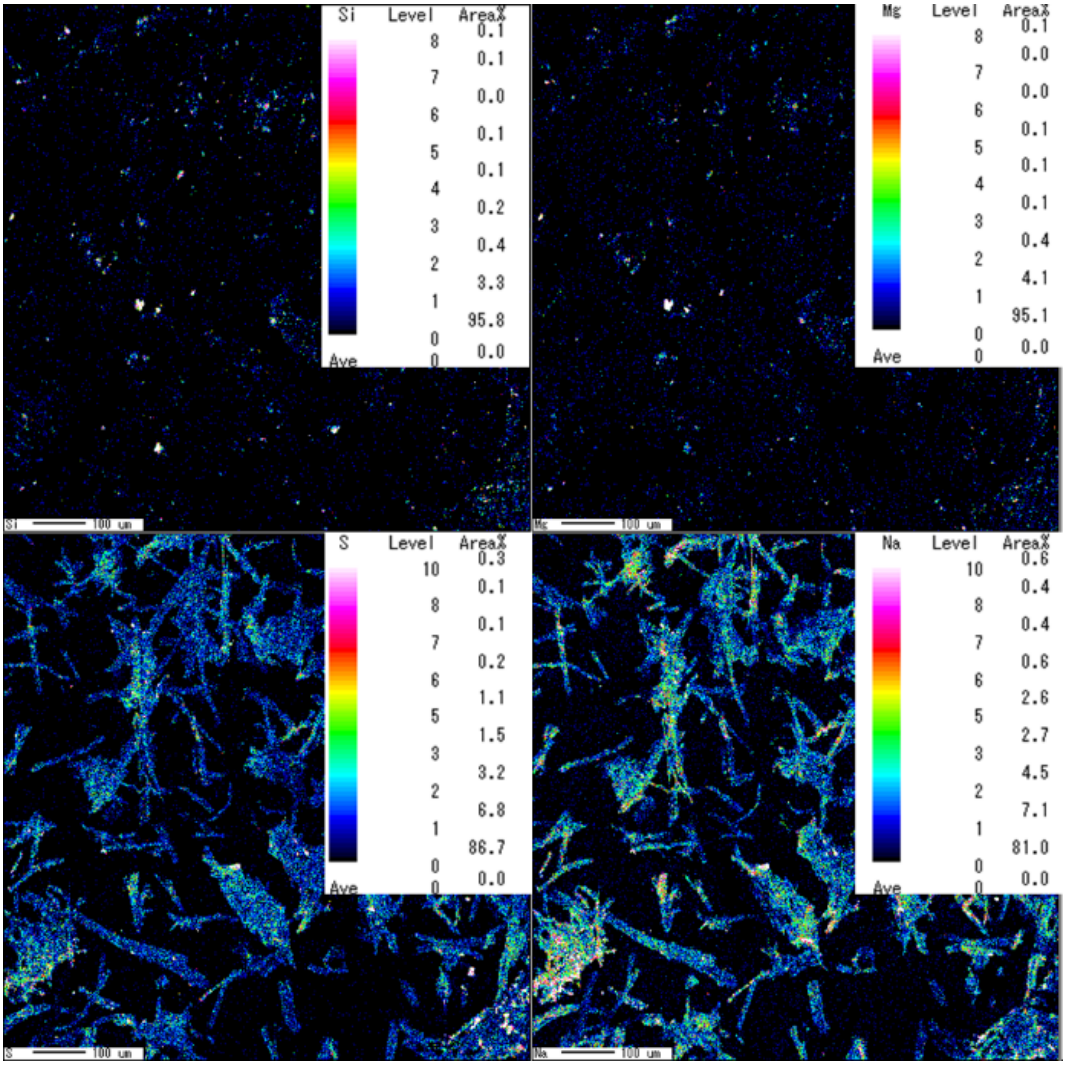

Figure 3 Detection of S and Na in “SA6345-2PN”.

Then, surface functional groups were detected by both FT-IR and XPS. In the results of FT-IR, characteristic peaks of cellulose were observed with C–O vibration at 1080 cm^{-1}, C–O–C in ring structure at 1130 cm^{-1}, and cellulose I and cellulose II at around 1400 cm^{-1}. A slightly increased intensity of the C–O–C bond with a decreased hydrolysis temperature was observed because of the removal of the amorphous region (Figure 4), though no significant changes in the FT-IR spectrum suggested no secondary products formed.

The sulfate groups introduced via sulfuric acid hydrolyzation were measured at a binding energy around 170 eV by XPS. An increased value of sulfate in SA6365-2PN was observed at a higher acid concentration and hydrolysis temperature (Figure 5). Also, a peak contributed by sodium at around 260 eV was detected in CNC samples and sample C, but not in hardwood pulp (the star mark in Figure 5), which suggested the existence of similar structure of the produced CNCs. However, the O1s peak of P-CNCs (taking SA6345-2PN as an example) shifted to the left, suggesting that P-CNCs contained sodium salts and absorbed more moisture [30–32] (Figure 6). However, neither SA6345-2PN nor SA4645-2PN showed an obvious sulfate peak. Instead, a high C/O ratio of SA6345-2PN (0.82) and SA4645-2PN (0.91) was found when it came to overall areas of O1s and C1s XPS signals. Whereas, C/O ratios of 0.78 and 0.61 were calculated for SA6365-2PN and sample C, respectively, which showed a peak of sulfate, indicating the presence of non-cellulosic materials as sulfate groups. Considering the results from both EPMA and XPS, the detected sulfate and sodium was more significant in SA6345-2PN, and most of them were suggested to exist as salts rather than forming sulfate groups on the surface. Not only might the efficiency of composite manufacturing be influenced, but the extra remaining salt might also lead to disadvantages, such as too much moisture absorption. For a longer shelf life and further usage, an improved preparation process is needed to remove most of the salt.

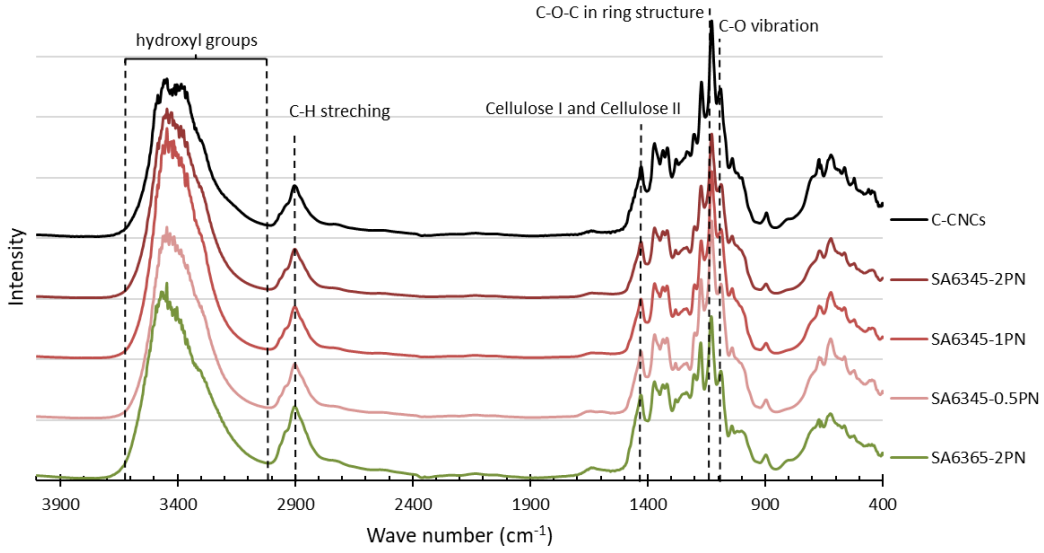

Figure 4 FT-IR spectra of C-CNCs and some of P-CNCs.

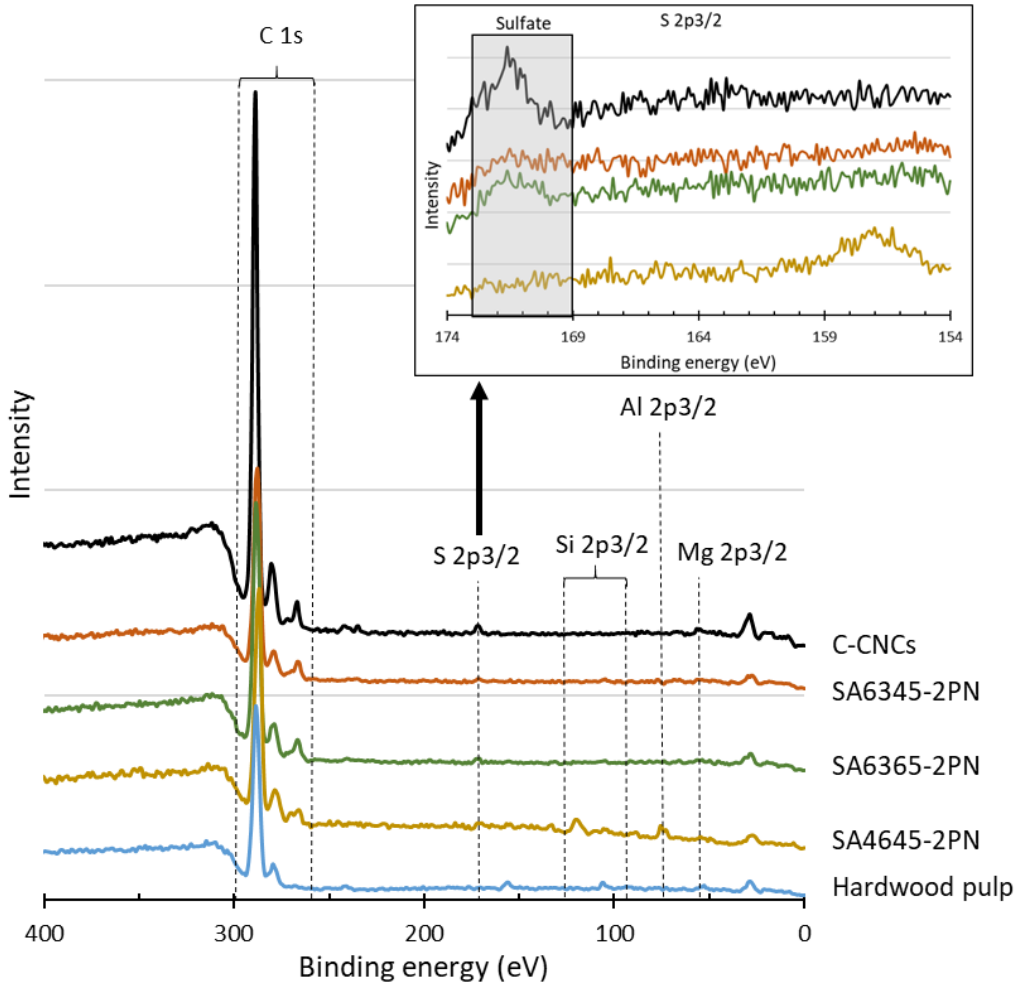

Figure 5 XPS spectrum and magnification of S2p3/2.

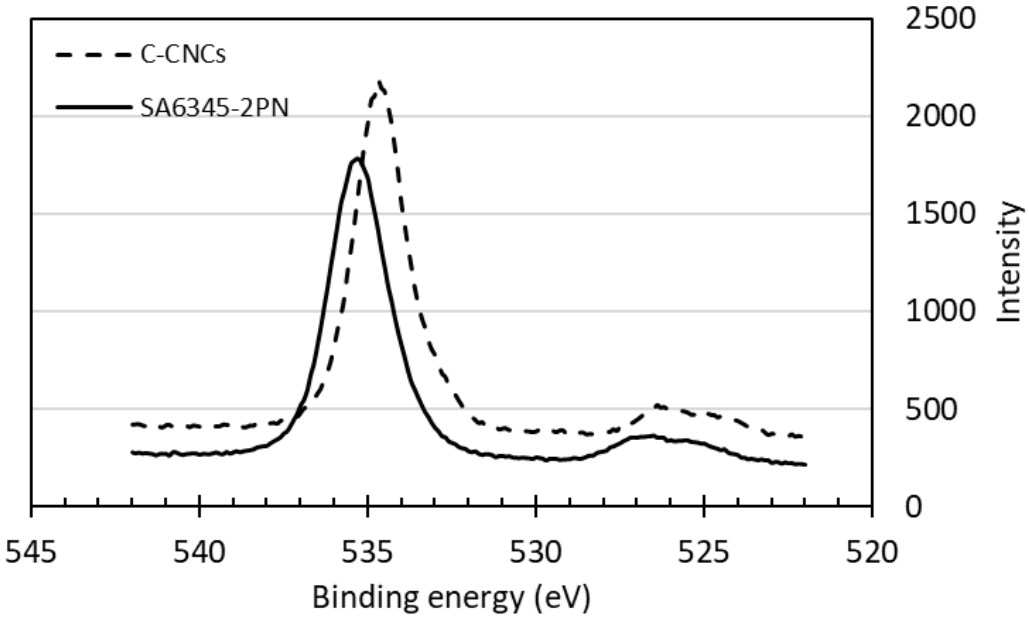

Figure 6 XPS spectrum of O1s in “SA6345-2PN” and C-CNCs.

2.4.3 Charging behavior and surface environment of C-CNCs

Sulfate groups dominated the colloidal behavior of CNCs with a pH-independent ζ value. Accordingly, potentiometric acid-base titration was applied to determine the charging behavior, which might be influenced also by sulfate groups. Surface charge of CNCs resulted in a difference between titration curves of the CNC suspension and blank solution. The surface charge density was defined with the specific surface area of 304.2 m^2/g obtained by dimensional information from TEM and an assumed cylindrical shape, with the assumption of a non-aggregated state.

Figure 7 shows that the surface charge density of CNCs was determined to be approximately -0.1 C/m^2 after avoiding possible error from the strongly curved titration curve at low pH, which is close to that of sulfate group grafted CNCs prepared via sulfuric acid hydrolysis. [19] As shown in Table 3, the detection of sulfur by elemental analysis also suggested the presence of sulfate groups on the surface of CNCs. By counting backward with the relationship between the surface charge density and sulfur content, entire dissociation of sulfate groups of CNCs were derived from the approximately same level of %S between the two methods. [2, 33]

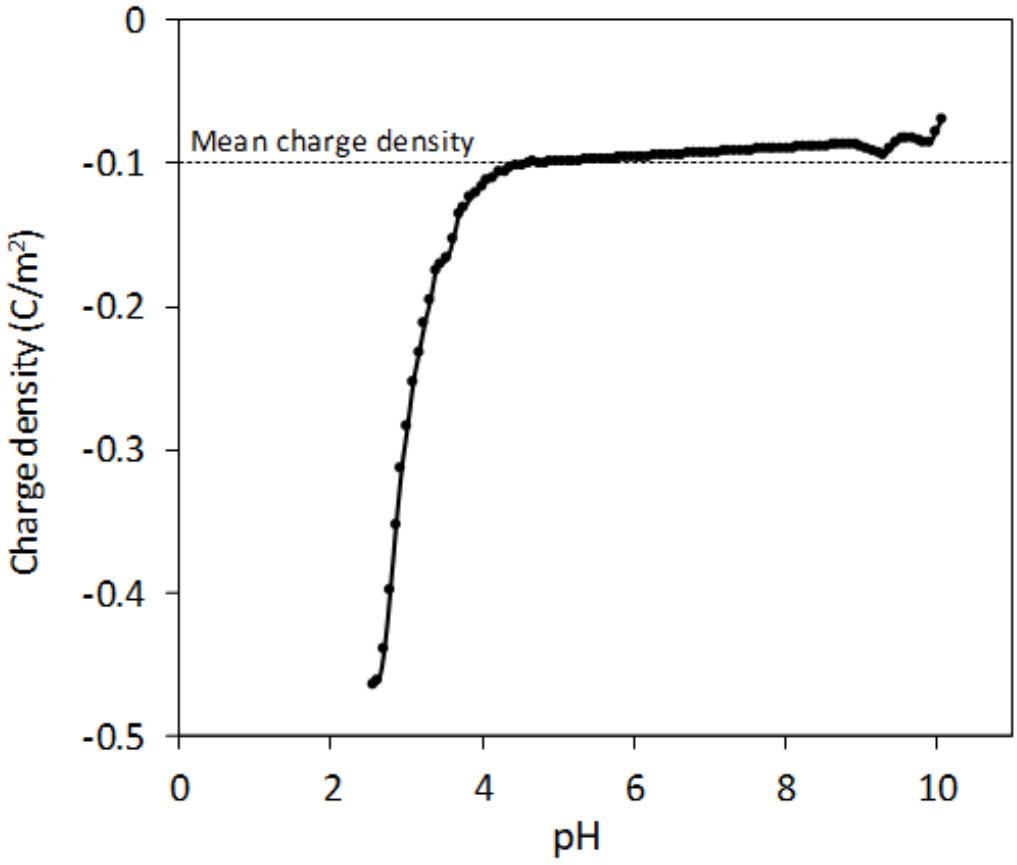

Figure 7 Surface charge density of C-CNCs.

Table 3 Elemental composition of C-CNCs.

Element	N	C	S	H
Ratio (wt.%)	0.26	39.63	0.97	6.27

2.4.4 Analysis of electrophoretic mobility of C-CNCs

In the calculation of electrophoretic mobility from theories ($\mu_{theoretical}$), it was assumed that the surface charge density was constantly -0.1 C/m^2 as shown in Figure 7 and previous studies[19, 33, 34]. Subsequently, the theories regarding orientation and the relaxation effect as well as the shape and surface potential of CNCs (eqns (1–3)) provided theoretical curves of $\mu_{theoretical}$. Figure 8 exhibits those theoretical curves for fitting to the $\mu_{measured}$ on the condition of the slipping plane located 0.60–0.75 nm away from the particle surface.

At low electrolyte concentrations, the Ohshima-Overbeek averaged equation and Ohshima-Overbeek perpendicular equation curves fairly fitted the data points better than the others. This confirmed the assumption that CNCs have highly charged surfaces, indicating that the relaxation of the double layer reduces μ. To be more exact, however, neither the Ohshima-Overbeek averaged equation nor the Ohshima-Overbeek perpendicular equation fitted the data points, but the experimental data remained between both equations.

The Ohshima-Overbeek perpendicular equation did not fit the data points exactly due to the cylindrical shape of CNCs, suggesting a possible orientation effect. ${\mu_{av}}^{OO}$ considers the orientation effect of CNCs, however, does not consider the end effect sufficiently. As mentioned before, ${\mu_{av}}^{OO}$ uses ${\mu_{\perp}}^{OO}$ as the perpendicular orientation with a relaxation of the double layer, but adopts μ_{smol}, in which the parallel part ignored the relaxation effect. This means that the Ohshima-Overbeek averaged equation is not completely suitable for cases with the significant end effect. The data points of $\mu_{measured}$ fell close to ${\mu_{av}}^{OO}$ at higher electrolyte concentrations or at higher κa values. With a relatively small double layer and a κa value greater than 3.5, a trend similar to the theoretical prediction was shown in experimental data, which meant that the end effect

became less pronounced. On the other hand, cellulose nanofibers are shaped as a long cylinder with relatively low ζ, if mechanically prepared, than CNCs and are reported to exhibit behavior predicted by "Ohshima-Overbeek perpendicular equation"[35], whereas the relatively short length and high surface zeta potential characteristic of CNCs was responsible for the difference between $\mu_{measured}$ and ${\mu_{av}}^{OO}$. In addition, a misinterpretation of the partial end effect consideration in the case of a relatively thick double layer when the same equations were applied was reported, and it was suggested that the end effect played a significant role in this situation. [20] Thus, another estimation was suggested in this reference to deal with such a short cylinder with a thick double layer and a non-negligible end effect, all characteristic of CNCs.

A concept to keep ${\mu_{\perp}}^{OO}$ as ${\mu_{av}}^{OO}(\kappa a)$ and replace μ_{smol} with ${\mu_{\perp}}^{OO}(\kappa L/2)$, where L is the length of the CNC particle, for a cylinder model oriented parallel to the field in calculating the averaged μ from Ohshima's equation (eqn (5)) proposed by Bakker et al.[22] was applied. Then, a motivation of ${\mu_{av}}^{OO\,(L)} = \frac{\left({\mu_{\perp}}^{OO}(\frac{\kappa L}{2})+2{\mu_{\perp}}^{OO}\right)}{3}$ was calculated and named as "Ohshima-Overbeek (length) equation". Figure 9 shows that this theory presented a much better fitting than Smoluchowski's theory for the parallel part. Nevertheless, the experimental data points were close to the Ohshima-Overbeek (length) equation, where the Ohshima equation was applied to both perpendicular and parallel parts for the cylinder mobility to account for the end effect.

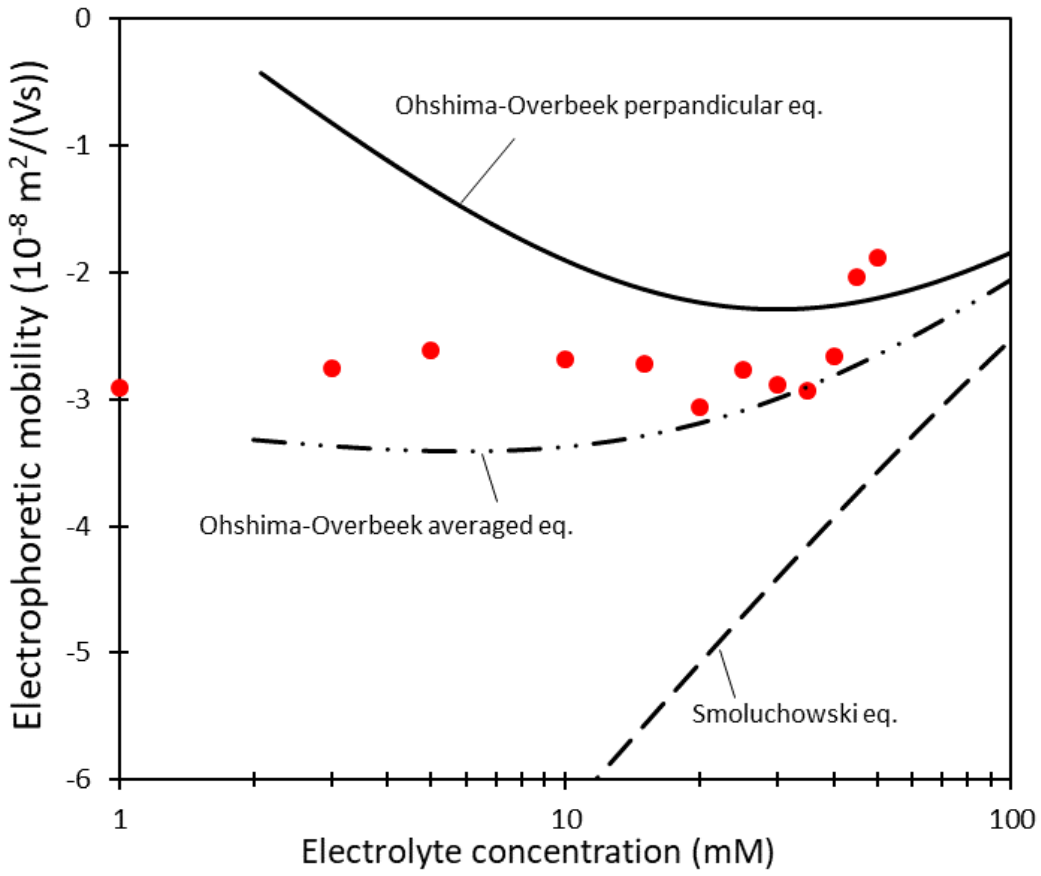

Figure 8 Fitting of theoretical equations when the surface charge density and distance between the particle surface and slipping plane are assumed to be -0.107 C/m^2 and 0.65 nm, respectively.

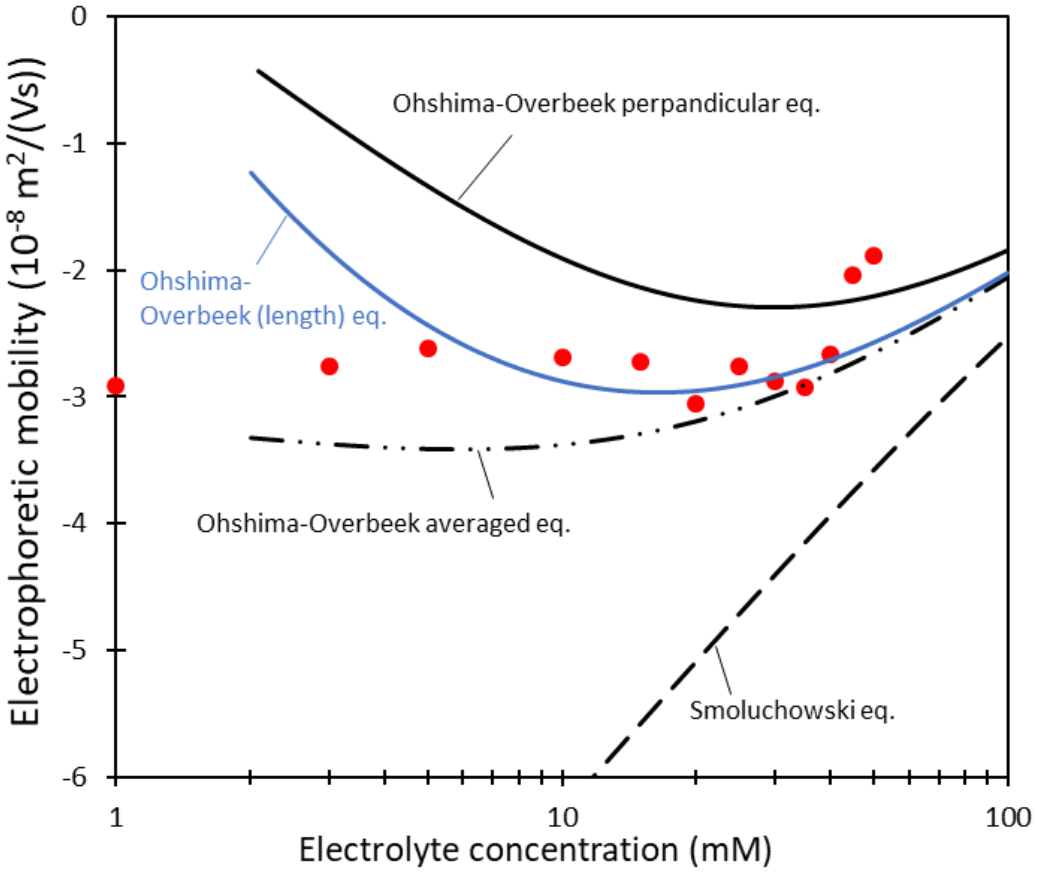

Figure 9 Fitting of theoretical equations including the Ohshima-Overbeek (length) equation as the best fitted approximation.

In addition, considering CNCs with various lengths, the “Ohshima-Overbeek (length) eq.” curve was confirmed to become closer to “Ohshima-Overbeek averaged eq.” with an increasing CNC length, suggesting that the end effect plays a major role for shorter CNCs.

Finally, our result suggests that the use of Smoluchowski's equation leads to the underestimation of ζ in magnitude. The relaxation effect and the end effect are crucial for parallel and perpendicular mobilities of CNCs due to high charge and a relatively small aspect ratio.

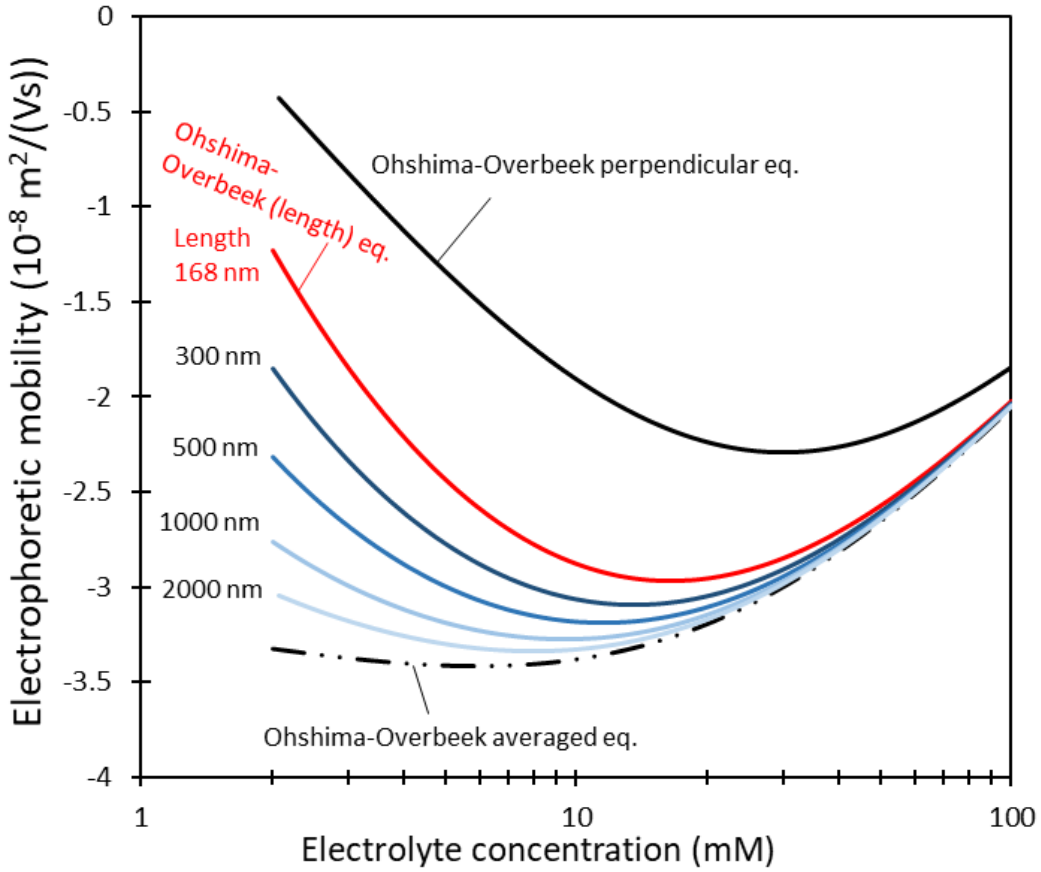

Figure 10 An effect of the CNCs length depicted with "Ohshima-Overbeek (length) eq." with an assumption that the radius, zeta potential, and surface charge density are constant (independent with the length of CNCs).

2.5 Conclusion

Dry hardwood pulps were used to prepare CNCs under controlled conditions. To introduce sulfate groups on CNCs, a high hydrolysis temperature (65 °C) was preferred to produce redispersible CNCs with successfully grafted sulfate groups. Through the results of potentiometric titration and elemental analysis, sulfate groups introduced via sulfuric acid hydrolysis were proposed to possess such a strongly negative surface potential. At lower electrolyte concentrations (< 25 mM), the double layer remained relatively thick and the suspensions did not aggregate. In this situation, theoretical results such as the Ohshima-Overbeek averaged equation and the Ohshima-Overbeek perpendicular equation explained the experimental data more accurately than Smoluchowski's equation, owing to the cylindrical shape of CNC colloidal particles and the relaxation effect caused by the highly charged surface from sulfate groups. The reason that neither the Ohshima-Overbeek averaged equation nor the Ohshima-Overbeek perpendicular equation fitted the experimental data accurately might be the end effect, which became remarkable in the case of a short cylinder with a remarkable surface charge. Dealing with this problem, we successfully determined μ more exactly from ζ by a new method based on the Ohshima-Overbeek (length) equation that has never been applied to CNCs before.

Reference

1 Bondeson, D.; Mathew, A.; Oksman, K. Optimization of the isolation of nanocrystals from microcrystalline cellulose by acid hydrolysis. *Cellulose* **2006**, *13*, 171–180.

2 Dong, X.M.; Revol, J.F.; Gray, D.G. Effect of microcrystallite preparation conditions on the formation of colloid crystals of cellulose. *Cellulose* **1998**, *5*, 19–32.

3 Abdul Khalil, H.; Davoudpour, Y.; Islam, M.N.; Mustapha, A.; Sudesh, K.; Dungani, R.; Jawaid, M. Production and modification of nanofibrillated cellulose using various mechanical process: A review. *Carbohydr. Polym.* **2014**, *99*, 649–665.

4 Beck-Candanedo, S.; Roman, M.; Gray, D.G. Effect of reaction conditions on the properties and behavior of wood cellulose nanocrystal suspensions. *Biomacromolecules* **2005**, *6*, 1048–1054.

5 Dong, H.; Strawhecker, K.E.; Snyder, J.F.; Orlicki, J.A.; Reiner, R.S.; Rudie, A.W. Cellulose nanocrystals as a reinforcing material for electrospun poly(methyl methacrylate) fibers: Formation, properties and nanomechanical characterization. *Carbohydr. Polym.* **2012**, *87*, 2488–2495.

6 Yanamala, N.; Farcas, M.T.; Hatfield, M.K.; Kisin, E.R.; Kagan, V.E.; Geraci, C.L.; Shvedova, A.A. In vivo evaluation of the pulmonary toxicity of cellulose nanocrystals: A renewable and sustainable nanomaterial of the future. *Acs Sustain. Chem. Eng.* **2014**, *2*, 1691–1698.

7 Beck, S.; Bouchard, J.; Berry, R. Dispersibility in water of dried nanocrystalline cellulose. *Biomacromolecules* **2012**, *13*, 1486–1494.

8 Espinosa, S.C.; Kuhnt, T.; Foster, J.; Weder, C. Isolation of thermally stable cellulose nanocrystals by phosphoric acid hydrolysis. *Biomacromolecules* **2013**, *14*, 1223–1230.

9 Pan, M.; Zhou, X.; Chen, M. Cellulose nanowhiskers isolation and properties from acid hydrolysis combined with high pressure homogenization. *BioResources* **2013**, *8*, 933–943.

10 Chen, L.; Wang, Q.; Hirth, K.; Baez, C.; Agarwal, U.P.; Zhu, J.Y. Tailoring the yield and characteristics of wood cellulose nanocrystals (CNC) using concentrated acid hydrolysis. *Cellulose* **2015**, *22*, 1753–1762.

11 Zhang, Y.; Lu, X.; Gao, C.; Lv, W.; Yao, J. Preparation and characterization of nanocrystalline cellulose from bamboo fibers by controlled cellulose hydrolysis. *J. Fiber Bioeng. Inform.* **2012**, *5*, 263–271.

12 Yu, H.; Qin, Z.; Liang, B.; Liu, N.; Zhou, Z.; Chen, L. Facile extraction of thermally stable cellulose nanocrystals with a high yield of 93% through hydrochloric acid hydrolysis under hydrothermal conditions. *J. Mater. Chem. A* **2013**, *1*, 3938–3944.

13 Yu, H.; Qin, Z.; Liang, B.; Liu, L.; Yang, X.; Zhou, Y.; Yao, J. Comparison of the reinforcing effects for cellulose nanocrystals obtained by sulfuric and hydrochloric acid hydrolysis on the mechanical and thermal properties of bacterial polyester. *Compos. Sci. Technol.* **2013**, *87*, 22–28.

14 Dufresne, A. **2013** Nanocellulose: from nature to high performance tailored materials. *Berlin/Boston, DE: De Gruyter*.

15 Bondeson, D.; Mathew, A.; Oksman, K. Optimization of the isolation of nanocrystals from microcrystalline cellulose by acid hydrolysis. *Cellulose* **2006**, *13*, 171–180.

16 Pan, J.; Hamad, W.; Straus, S.K. Parameters affecting the chiral nematic phase of nanocrystalline cellulose films. *Macromolecules* **2010**, *43*, 3851–3858.

17 Hasani, M.; Cranston, E.D.; Westman, G.; Gray, D.G. Cationic surface functionalization of cellulose nanocrystals. *Soft Matter* **2008**, *4*, 2238–2244.

18 Prathapan, R.; Thapa, R.; Carnier, G.; Tabor, R.F. Modulating the zeta potential of cellulose nanocrystals using salts and surfactants. *Colloids and Surfaces A: Physicochemical and Engineering Aspects* **2016**, *509*, 11–18.

19 Zoppe, J.O.; Xu, X.; Känel, C.; Orsolini, P.; Siqueira, G.; Tingaut, P.; Zimmermann, T.; Klok, H-A. Effect of surface charge on surface-initiated atom transfer radical polymerization from cellulose nanocrystals in aqueous media. *Biomacromolecules* **2016**, *17*, 1404–1413.

20 Ohshima, H. Approximate analytic expression for the electrophoretic mobility of moderately charged cylindrical colloidal particles. *Langmuir* **2015**, *31*, 13633–13638.

21 van der Drift, W.P.J.T.; de Keizer, A.; Overbeek, J.Th.G. Electrophoretic mobility of a cylinder with high surface charge density. *Journal of Colloid and Interface Science* **1979**, *71*(1), 67–78.

22 Bakker, H.E.; Besseling, T.H.; Wijnhoven, J.E.G.J.; Helfferich, P.H.; van Blaaderen, A.; Imhof, A. Microelectrophoresis of silica rods using confocal microscopy. *Langmuir* **2017**, *33*, 881–890.

23 Reid, M.S.; Villalobos, M.; Cranston, E.D. Benchmarking cellulose nanocrystals: From the laboratory to industrial production. *Langmuir* **2017**, *33*, 1583–1598.

24 Dong, S.; Bortner, M.J.; Roman, M. Analysis of the sulfuric acid hydrolysis of wood pulp for cellulose nanocrystal production: A central composite design study. *Industrial Crops and Products* **2016**, *93*, 76–87.

25 Aguayo, M.G.; Pérez, A.F.; Reyes, G.; Oviedo, C.; Gacitúa, W.; Gonzalez, R.; Uyarte, O. Isolation and characterization of cellulose nanocrystals from rejected fibers originated in the kraft pulping process. *Polymers* **2018**, *10*, 1145.

26 Sacui, I.A.; Nieuwendaal, R.C.; Burnett, D.J.; Stranick, S.J.; Jorfi, M.; Weder, C.; Foster, E.J.; Olsson, R.T.; Gilman, J.W. Comparison of the properties of cellulose nanocrystals and cellulose nanofibrils isolated from bacteria, tunicate, and wood processed using acid, enzymatic, mechanical, and oxidative methods. *Acs Appl. Mater. Interfaces* **2014**, *6*, 6127–6138.

27 Moon, R.; Beck, S.; Rudie, A. Cellulose nanocrystals – a material with unique properties and many potential applications. *Production and Applications of Cellulose Nanocrystals*, TAPPI PRESS, United States of America. **2013**, 9–12.

28 Ohshima, H. Surface charge density/ surface potential relationship for a cylindrical particle in an electrolyte solution. *Journal of Colloid and Interface Science* **1998**, *200*, 291–297.

29 Bhattacharyya, S.; De, S. Numerical study of the influence of solid polarization on electrophoresis at finite Debye thickness. *Physical Review E* **2015**, *92*, 032309.

30 Hurtta, M.; Pitka¨nen, I.; Knuutinen, J. Melting behavior of D-sucrose, D-glucose, and D-fructose. *Carbohydrate Research* **2004**, *339*, 2267–2273.

31 Rosenthal, D.; Ruta, M.; Schlögl, R.; Kiwi-Minsker, L. Combined XPS and TPD study of oxygen-functionalized carbon nanofibers grown on sintered metal fibers. *Carbon* **2010**, *48*, 1835–184.

32 Abu Haija, M.; Guimond, S.; Uhl, A.; Kuhlenbeck, H.; Freund, H.J. Adsorption of water on thin V_2O_3(0 0 0 1) films. *Surface Science* **2006**, *600*, 1040–1047.

33 Abitbol, T.; Kloser, E.; Gray, D.G. Estimation of the surface sulfur content of cellulose nanocrystals prepared by sulfuric acid hydrolysis. *Cellulose* **2013**, *20*, 785–794.

34 Kobayashi, M. Electrophoretic mobility of latex spheres in the presence of divalent ions: experiments and modeling. *Colloid and Polymer Science* **2008**, *286*, 935–940.

35 Sato, Y.; Kusaka, Y.; Kobayashi, M. Charging and aggregation behavior of cellulose nanofiber in aqueous solution. *Langmuir* **2017**, *33* (44) 12660–12669.

Chapter 3

Development of Robust Conductive Tracks by Undercoating Cellulose Nanocrystal-formulated Ink

3.1 Abstract

Coatings are usually applied on paper for improving ink penetration or pigment retention. To deal with the complex surface environment of paper which might bring disadvantages to the adhesion among conductive ink particles, the applicability of cellulose nanocrystals (CNCs) were tested as a pre-treatment of paper surface. A CNC suspension, exactly like an aqueous-based ink, was printed on a paper surface to be a few layers. Then, the CNC-undercoated substrates were examined on the silver nanoparticles ink (AgNPs ink)-wettability, surface texture, and roughness. Resistance of the printed silver tracks was measured, and a friction test were conducted to evaluate the adhesion.

3.2 Introduction

In several research practices, inkjet printing was selected to introduce functional inks onto paper substrates for the reduced cost, controllability, high throughput, and milli- to micro-meter scale patterning. [1–3] As inkjet is not a new technology in the world, the operation method of inkjet printing has been developed well with an easily controlled system and a potential for high throughput. In addition, it is possible to deposit different materials simultaneously by inkjet, which is advantageous in mixing multiple solutions in small quantities. [4, 5]

With the consideration of environment and demand of flexible devices, paper is regarded as a suitable material being the substrate of printed functional inks. However,

as mentioned in Chapter 1, the porous structure, rough surface, and complex surface chemistry would decrease the performance of functional applications like printed electronics. Other problems such as increased cost and difficulty in recycling would occur through a plastic film is laminated on paper to deal with the disadvantages of paper surface. [6] Also, pigments and surface coating on commercially-available inkjet paper might decrease the thermal stability of the whole paper, which is not suitable for conductive ink printing.

The aim of this study is to seek an eco-friendly surface treatment of paper substrates to prevent the drawbacks caused by the roughness and uncertain chemical environments. Nano-scaled bundles of crystalline regions of cellulosic chains, CNCs, was chosen to be introduced on paper as an undercoat. Comparing with the complex surface chemistry environment of paper, CNCs have the potential to improve the robustness of the tracks thanks to the identified structure. Moreover, CNCs prepared via sulfate acid hydrolysis exhibit excellent dispersibility in water. Highly charged sulfate groups of CNCs with the extracting process of sulfuric acid hydrolysis induced an electrostatically stability in aqueous solution as investigated in Chapter 2. That means CNCs have potentials to be applied as an aqueous ink, which is non-toxic and eco-friendly.

Contact angles between ink and the surface of substrates were measured to evaluate the ink-wettability. As the surface smoothness is also important, the roughness of a paper surface with or without CNCs printed was measured with a scanning probe microscope (SPM). In the measurement, the sample surface was scanned with a probe to compose profile images. An interaction between the probe and sample surface influences the normal attractive force occurring between them. By monitoring the changes in the amplitude of the attractive force, the surface topography can be obtained. Furthermore, cross-sections of CNCs-printed paper samples were observed, and a

friction test was conducted to study the adhesion between the conductive ink and substrates.

3.3 Experimental

3.3.1 Sample preparation

Commercially available CNCs prepared by sulfuric acid hydrolysis (University of Maine, USA) was used as a functional ink after homogenizing in water. Inkjet printing was done by using a material inkjet printer (Dimatix DMP-2831, Fujifilm, Japan). To prevent curling of paper samples due to high contents of moisture absorbed from CNC inks and strong shrinkage force resulting during drying, photo-grade inkjet paper with silica formed on a resin coat base was chosen. Thus, "EPSON CRISPIA" was chosen as the substrate owing to a high picking resistance, quick absorption of inks and high dimensional stability.

A CNC suspension with a concentration of 0.1% (w/w) was loaded into a cartridge and the ejection voltage was set to 40 V to print CNC coatings to 1, 5, 10, and 15 layers (C1–C15) on paper substrates. Additionally, a silver layer was introduced on the CNC coatings with the water-based silver nanoparticles ink (W-AgNPs ink; NBSIJ-MU01, Mitsubishi paper mills Ltd., Japan) (Figure 11).

3.3.2 CNC properties

The outward appearance of CNCs was investigated by transmission electronic microscopy (TEM; JEM-1200 EXII, JEOL, Japan). CNC suspensions at 0.1% (w/w) were dropped on 20 mesh carbon coated TEM copper grids for TEM observations at 60 kV. The particle dimensions were analyzed using *ImageJ* (https://imagej.nih.gov/ij/index.html) for at least 30 different particles. Only individual particles with clear edges were measured, and the width was determined as the diameter in the center of each particle.

3.3.3 Ink-wettability of CNC pre-printed samples

Ink-wettability was studied by measuring the contact angle by a contact angle meter (DMs-401, Kyowa Interface Science Co., Ltd., Japan). The contact angles between a 0.5 μL W-AgNP drop and substrates were measured by image analysis each 100 ms by a contact angle meter (DMs-401, Kyowa Interface Science Co., Ltd., Japan).

3.3.4 Topographical observation of CNC pre-printed samples

SPM (E-sweep, Hitachi High-Tech Science, Japan) was used for the surface profile observation. The dynamic force mode (DFM) and a cantilever "SI-DF20" was chosen for 10 μm square samples that were measured at various magnifications. In addition, the sampling intelligent scan (SIS) mode was applied when the intervals between data points were too small to achieve high quality and prevent the damage of the probe as well. Then, the roughness value (*Ra*) was collected after scanning.

3.3.5 Surface appearance

A field emission scanning electron microscopy (FE-SEM; SU-8020, Hitachi-hightech, Japan) was applied to observe the surface structure of paper, CNC-printed surface, and W-AgNP-printed surface. Samples were cut into small pieces and attached onto a SEM sample holder with a double-sided, conductive, and adhesive carbon tape. Then, platinum was sputtered to coat samples to *ca.* 12 nm in thickness. The accelerating voltage of FE-SEM ranged from 1 mV to 10 mV in observation for whole viewing and detail observation. to observe the ink penetration depth, cross sections of samples were cut at 45° (Figure 12), placed onto a sample holder with a carbon tape, and then coated with sputtered platinum.

3.3.6 Evaluation of the improved W-AgNP area

The adhesive property between silver tracks and paper substrates was studied by the friction method as shown in Figure 13. A #3000 sandpaper was attached to the bottom of the arm with a 50 g weight. Then, the movable stage was moved back and forth to rub a sample against the sandpaper for several times. Pictures of the W-AgNP-

remaining area after 1, 3, 5, 10, 20, 30, 40, and 50 strokes of frictions were captured and compared to those before friction. At the same time, the electric resistance of printed W-AgNP area was measured with a four-point resistance meter.

3.4 Result and discussion

3.4.1 Ink-wettability of samples

The paper surface with CNCs was found to have higher ink-wettability from the measurement of the contact angle between the W-AgNPs ink and paper surfaces. Even on only one layer of CNCs ("C1"), the contact angle was approximately 33°, whereas that without CNCs ("no CNC") showed a contact angle approximately 45°, as shown in Figure 14. This result is in agreement with the previous study that paper surface with multiple layers of CNCs had a more polar component and enhanced the wetting by a polar liquid such as W-AgNPs ink. [7]

3.4.2 Roughness evaluation

With several printed CNCs, a lower roughness than photo-grade inkjet paper (named "no-CNC" in Figure 15) was observed. One to ten-layers were recommended for CNC pre-printing to maintain or decrease the surface roughness. In other words, a small amount of CNCs is capable of decreasing the surface roughness. Consequently, optimal ink-wettability was realized by printing CNCs on paper surfaces to obtain higher smoothness. This improvement was achieved by the nanoscale of CNCs.

3.4.3 Interaction between a silver track and printed CNCs

The robustness of the silver layer printed on the underlaid CNCs was measured and a reinforcement owing to CNC undercoats was suggested (Figure 16). With an increasing number of CNCs undercoats, more silver nanoparticle layer remained after frictions. The composition of the W-AgNPs ink is supposed to contribute the interaction with CNCs, and there might be intermolecular force that occurs between silver and cellulose.

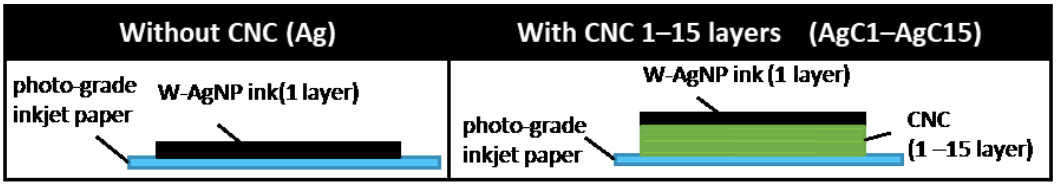

Figure 11 Side view of printed samples.

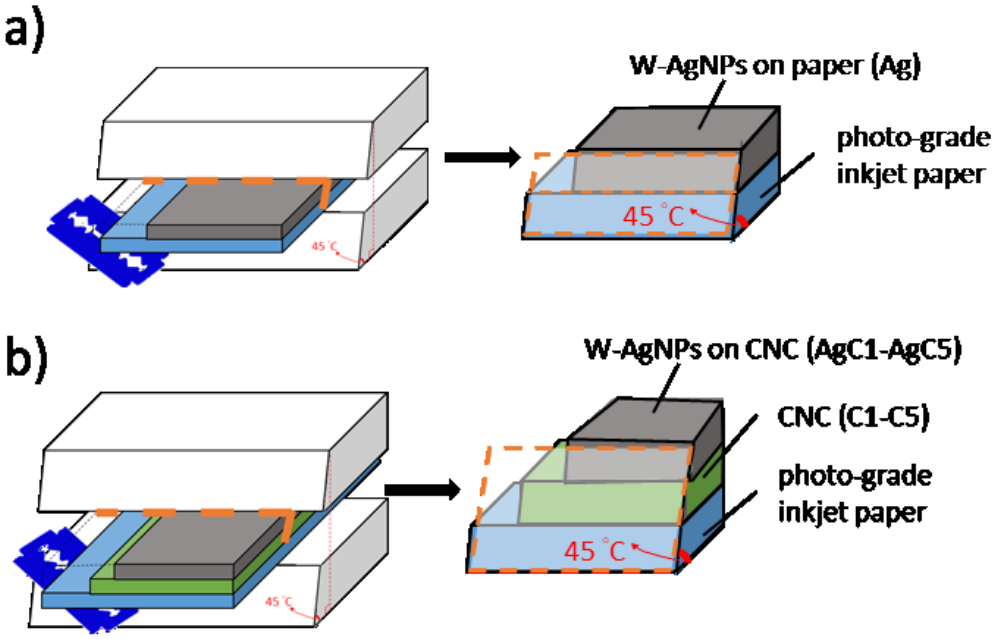

Figure 12 Schematic of SEM samples without CNCs (a) and with CNCs (b).

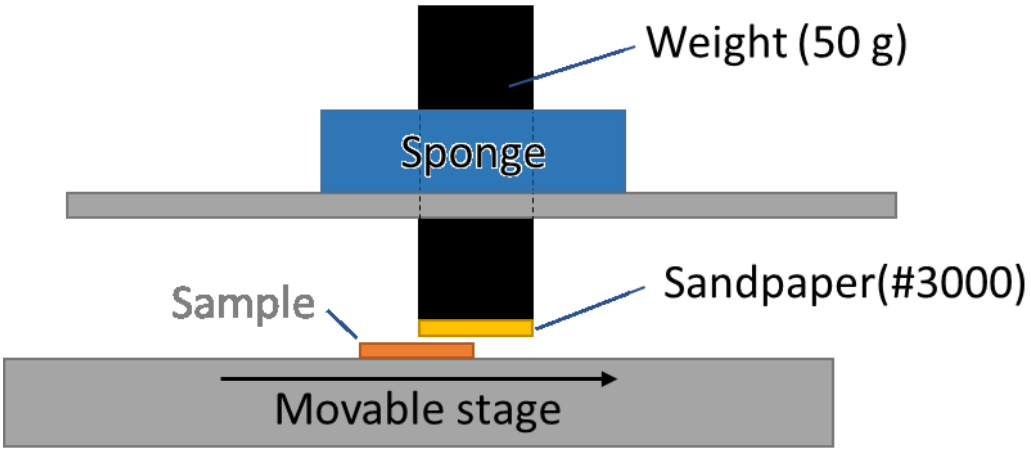

Figure 13 Schematic of how to subject W-AgNP-printed surface to friction.

3.4.4 Electrical performance of printed silver area

With the increased number of CNCs layers, the resistance of the silver layer increased before friction but obviously decreased after friction with a minimum at five layers (Figure 17). Furthermore, silver on 5-layer of CNC undercoats (AgC5) kept the highest conductivity. Consequently, CNC undercoats helped to form a robust layer of silver and thus kept the conductivity.

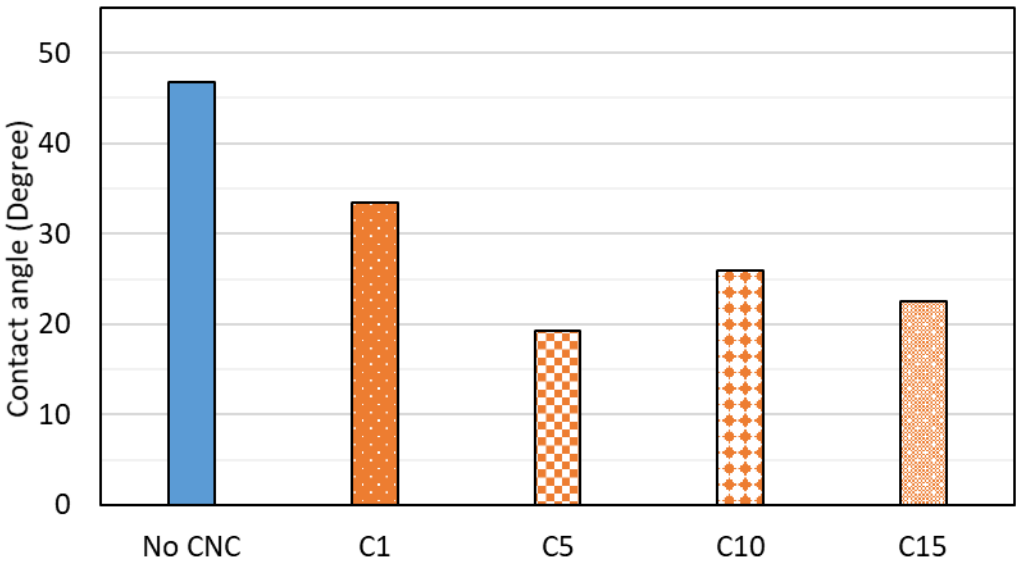

Figure 14 Contact angles of W-AgNPs ink on photo-grade inkjet paper with no CNCs (No CNC), 1 layer (C1), 5 layer (C5), 10 layer (C10), and 15 layer (C15) CNCs printed.

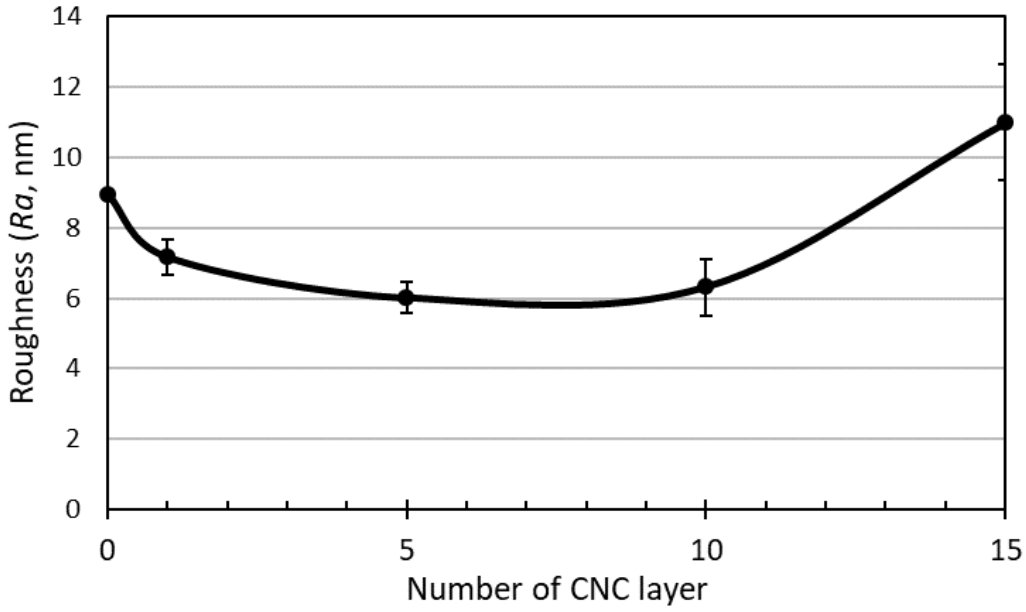

Figure 15 Roughness values of samples with a scanned area of a 10 μm square.

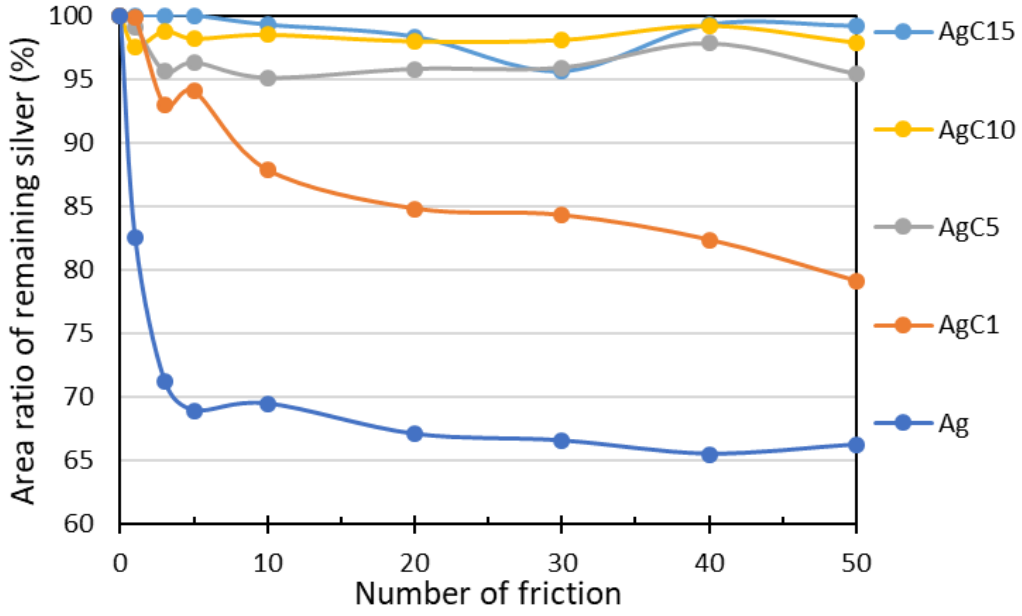

Figure 16 Area ratio of silver nanoparticle layer remaining after frictions.

3.4.5 Surface appearance

Different surface textures among three different top layers: an ink-receptive layer of the inkjet paper, printed monolayer CNCs (C1), and printed mono-layer W-AgNPs ink on CNCs (AgC1) were observed by SEM as shown in Figure 18. Paper surfaces are covered with mesoporous silica particles with a diameter of approximately 50 nm, CNCs spindles, and aggregated W-AgNPs, respectively.

Large cracks might have been caused when the cross section was cut; however, Figure 19 implies there are sufficiently large pores between silica particles to absorb the solvent through a CNC layer to solidify it by capillary force. Figure 20-a shows that a cross section of a W-AgNP layer *ca.* 6 μm in depth printed on CNCs. Then, a deeper penetration of W-AgNPs ink was found with a more CNC layer, suggesting an anchoring effect happened between CNCs and W-AgNP layer (Figure 21). Consequently, a CNC layer was found to build a dense structure owing to capillary force, and then ink anchoring was improved owing to CNC undercoats.

Also, during the sample cutting, the razor blade damaged the cross section and caused breakup. Some strap-shaped connecting structures are observed between silver and CNC layers as denoted by arrows. However, neither silver layer nor the connecting structure between silver and paper was found on the surface with CNCs unprinted. Silver printed directly on the paper was broken in cutting the cross section. Figure 22 showed that the surface mesoporous silica maintained its structure after the W-AgNP layer peeled off (Figure 22-c), suggesting a weak connection between the W-AgNP layer and paper surfaces.

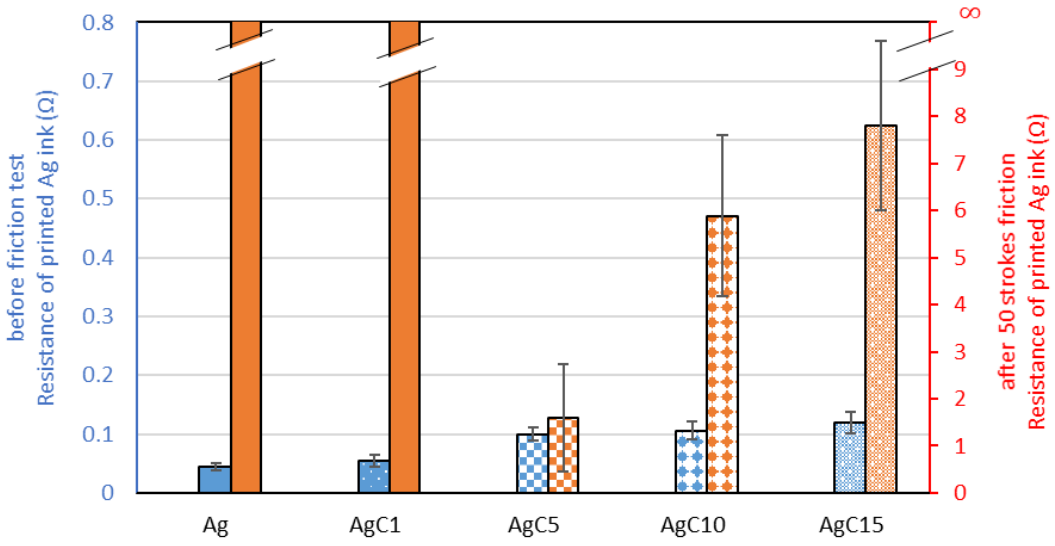

Figure 17 Resistance of silver layers before (left) and after friction (right).

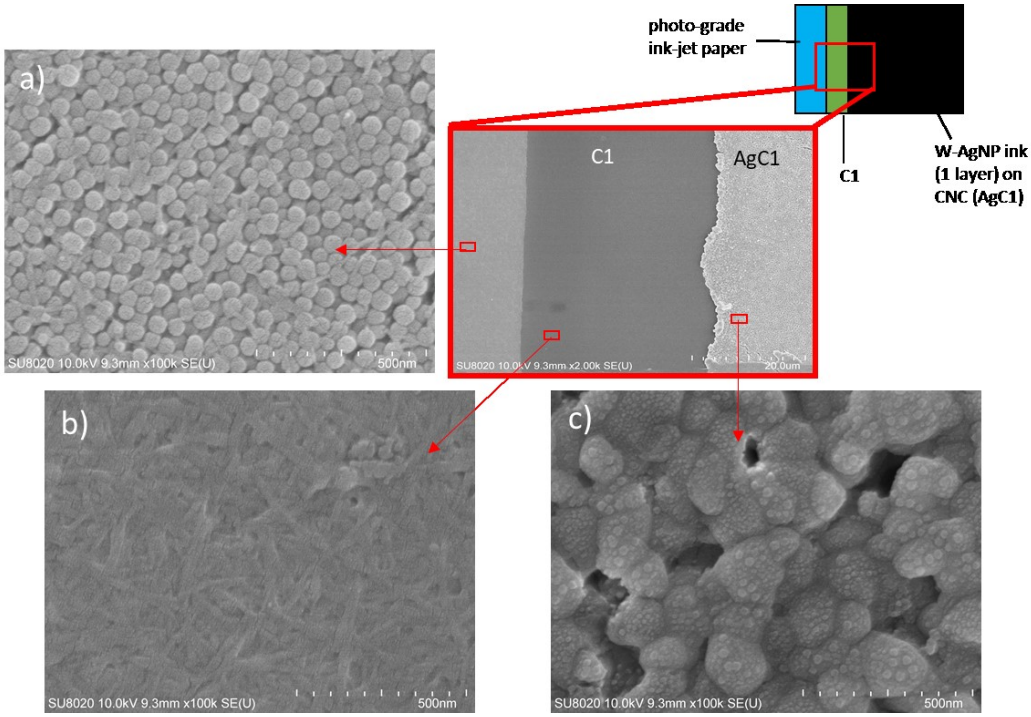

Figure 18 Surface structure of the three areas: (a) paper surface, (b) printed CNCs, and (c) printed W-AgNPs.

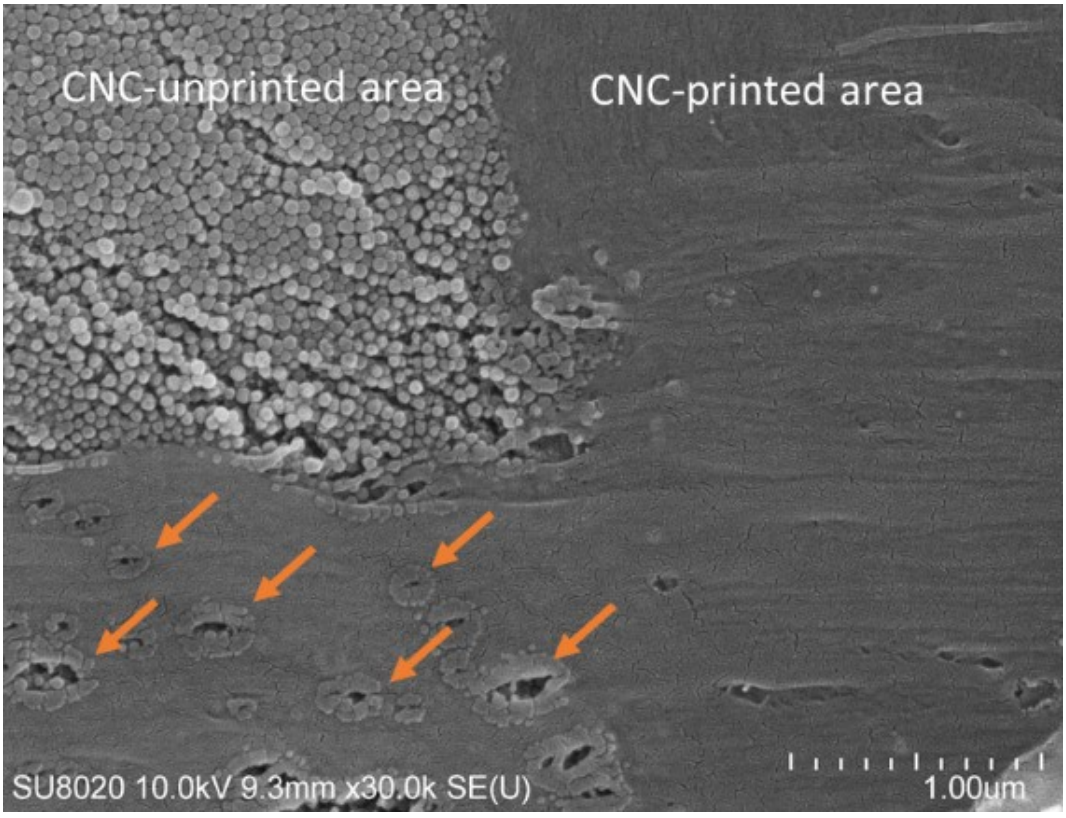

Figure 19 Cross section of CNC-unprinted/printed area.

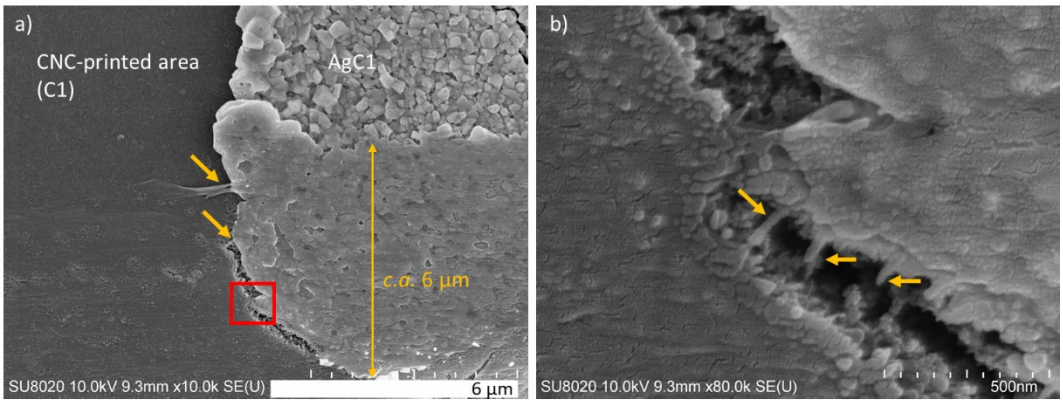

Figure 20 Cross section between CNC-printed area (C1)/AgC1: (a) whole view and (b) close-up of the red rectangle in (a) with strap-shaped structures denoted by arrows.

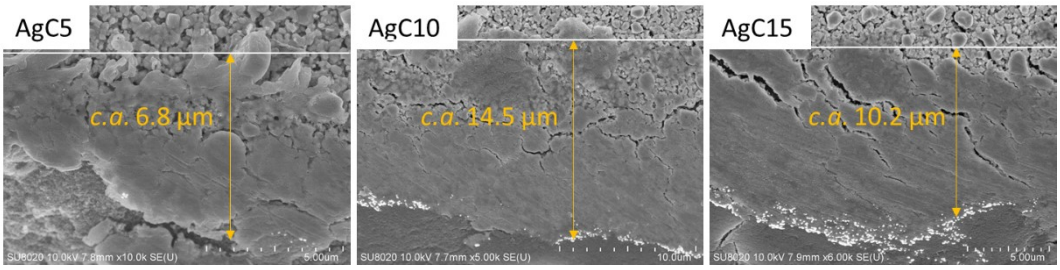

Figure 21 Penetration of W-AgNP ink on different layers of CNC undercoats.

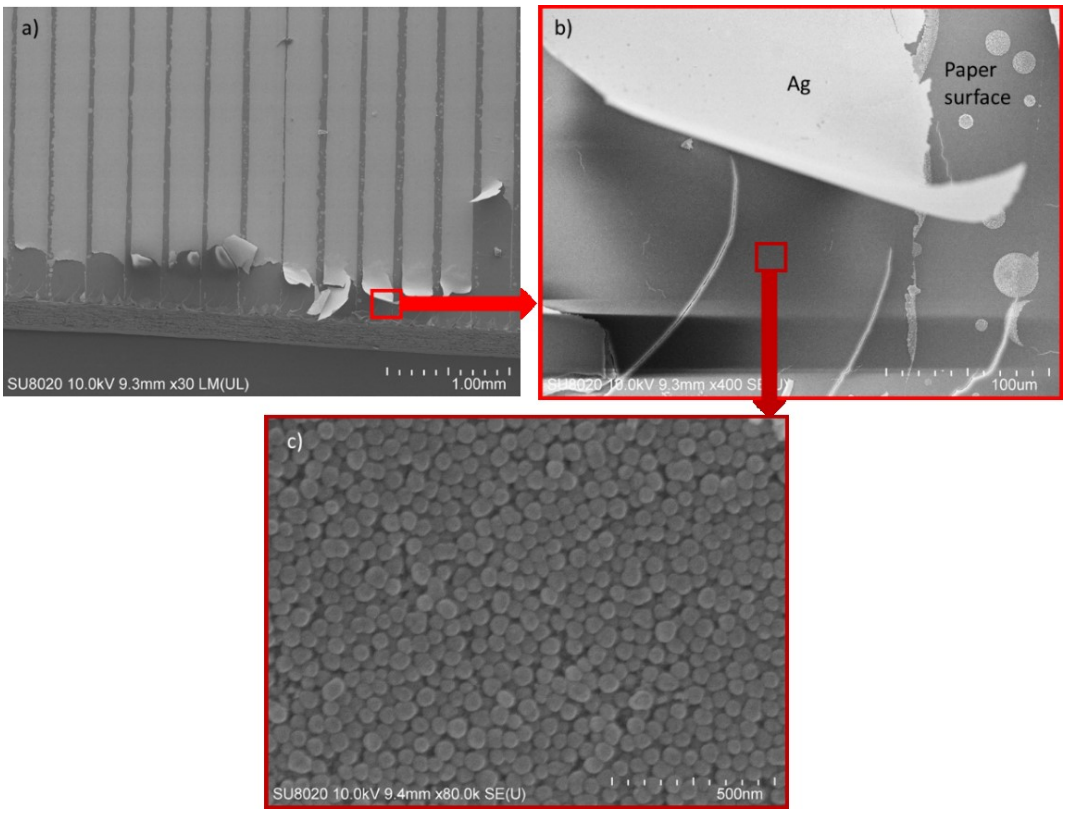

Figure 22 Silver without printed CNCs: (a) damage caused by cutting, (b) Silver layer peeled off, and (c) inkjet paper surface after the silver layer peeled off.

3.5 Conclusion

Undercoating of a reinforcement on the photo-grade inkjet paper was tried to support a printed silver layer with high electroconductivity and resistance to deformation. CNCs were chosen to apply on the inkjet paper surface as an adhesive between paper and ink. Because of a strong surface charge density and nano-scale dimensional smallness, CNCs were successfully applied as a water-based ink, letting them be easily used to create undercoats on paper surfaces by inkjet printing technology. Printed CNCs provided a better W-AgNPs ink receptivity to inkjet paper surfaces. Moreover, CNC undercoats facilitated W-AgNPs ink penetration and thus produced a firm and robust W-AgNP layer because of anchoring effect, reducing a better adhesion between the W-AgNPs ink and the substrates. An adequate amount of CNCs, five layers of CNCs for this case, was presented to control roughening of the paper surface and lead to a robust conductive track by penetration of a certain portion of the ink. Consequently, CNCs helped with W-AgNPs ink penetration and thus induced a firm and robust silver layer; therefore, for a better conductive performance of paper-based conductive layers, CNCs were suggested to be applied as a functional undercoat.

Reference

1 Minemawari, H.; Yamada, T.; Matsui, H.; Tsutsumi, J.; Haas, S.; Chiba, R.; Kumai, R.; Hasegawa, T. Inkjet printing of single-crystal films. *Nature* **2011**, 475.

2 Perelaer, J., de Laat, A.W.M.; Hendriks, C.E.; Schubert, U.S. Inkjet-printed silver tracks: low temperature curing and thermal stability investigation. *Journal of Materials Chemistry* **2008**, *18*, 3209–3215.

3 de Gans, B-J.; Duineveld, P.C.; Schubert, U.S. Inkjet printing of polymers: state of the art and future developments. *Advenced Materials* **2004**, *16* (3), 203–213.

4 Roth, E.A.; Xu, T.; Das, M.; Gregory, C.; Hickman, J.J.; Boland, T. Inkjet printing for high-throughput cell patterning. *Biomaterials* **2003**, *25*, 3707–3715.

5 Srimongkon, T.; Ishida, T.; Igarashi, K.; Enomae, T. Development of a bacterial culture system using a paper platform to accommodate media and an ink-jet printing to dispense bacteria. *American Journal of Biochemistry and Biotechnology* **2014**, *10* (1), 81–87.

6 Andersson, P.; Nilsson, D.; Svensson, P-O.; Chen, M.; Malmström, A.; Remonen, T.; Kugler, T.; Berggren, T. Active matrix displays based on all-organic electrochemical smart pixels printed on paper. *Advanced Materials* **2002**, *14*, 1460.

7 Ihalainen, P.; Määttänen, A.; Järnström, J.; Tobjörk, D.; Österbacka, R.; Peltonen, J. Influence of surface properties of coated papers on printed electronics. *Industrial & Engineering Chemistry Research* **2012**, *51* (17), 6025–6036.

Chapter 4

Fabrication of Cellulose Nanocrystal-based Transparent Conductive Device

4.1 Abstract

Instead of commercially available paper, cellulose nanocrystals (CNCs) were used as the main material to cast transparent films in various grammage and additional cellulose nanofibers (CNFs) in this Chapter. The fabricated films were characterized by transparency, mechanical property, as well as wettability. Then, oil-based conductive ink was printed on the films and annealed at 110°C. The resistance of tracks printed on the films were low enough to apply as a circuit.

4.2 Introduction

Considering a wider application of a transparent conductive device and an optimal conductivity brought by metallic inks which form interconnected phase after annealing, commercially available photo-grade inkjet paper used in Chapter 3 was not recommended. Instead, pure cellulosic material in nanoscale like CNCs, are expected to fabricate transparent and heat resistant casting films.

CNCs were believed to show liquid crystal behavior under certain concentration owing to the electric repulsion between CNC particles which promotes the orientation of them. [1] In Chapter 2, it was shown that sulfate groups with a strong negative charge were introduced onto CNCs during preparation with sulfuric acid hydrolysis. A high surface charge and small aspect ratio of CNCs were confirmed to obscure the chiral morphology and lead to the formation of a nematic phase. [1–3] It was reported that the onset concentration for liquid crystalline ordering of a CNC suspension was shifted to

higher concentrations than the predictions based on Onsager model. [4] In the Onsager model, the required volume fraction for liquid crystal formation and the aspect ratio of a cylinder is inversely proportional. However, in Chapter 2, it was suggested that a high surface charge caused electrostatic repulsion between the charged CNC cylinders and thus increased the effective volume fraction. On the other hand, ions interact strongly with the surface of CNC cylinders, and that might also be the reason that the effective cylinder shape and size of CNCs were outside the scope of the Onsager model. [1, 4]

Furthermore, a cholesteric helix ordering was developed while casting CNC suspensions because of the maintaining of alignment. [2] The influence of electrostatic repulsion was suggested to not only take place on liquid crystal formation but also on the pitch of cholesteric helix. [1] Pan *et al.* (2010) [4] reported the drying process of a CNC film and the formation of chiral nematic phase roughly are as below: During drying, when the concentration of CNCs was increased, a chiral nematic phase was formed, displaying characteristics of a cholesteric liquid crystal. After the critical concentration was reached, the disruption of the cholesteric phase in CNC suspensions formed helically twisted cylinders. Then, owing to the increased suspension concentration, the formation of more anisotropic phase was promoted. Upon full drying of the suspension, the cylinders were found to remain in the arrangement, and the interference with the interaction of CNC cylinders did not take place during drying process. An increased pitch was observed in the films; whereas the effect on crystallinity was not significant.

The aim of this study is to seek an eco-friendly material as the base of a transparent electric circuit without the drawbacks caused by a limited thermal stability and uncertain chemical environment like commercially-available inkjet paper. Regarding to the literature review above, CNC-films with interest optical properties and thermal stability have potentials to be produced by casting a CNC suspension. CNCs are

reported to bare a high temperature, and the sulfate groups are suggested to act as flame retardants when the temperature reached 300°C [5]. Such an ideal thermal stability also suggests CNCs be used as a substrate for conductive inks which exhibit an excellent conductivity but require annealing. However, CNCs were reported as short cylinders with a low aspect ratio above. Dimensional limitation is suspected to bring a disadvantage in mechanical strength to a pure C-film. Considering the compatibility between the hydrophilic CNCs and reinforcement, TEMPO (2,2,6,6-tetra-methylpiperidine-1-oxyl)-oxidized cellulose nanofibers (CNFs) were selected and expected to bring improved mechanical properties of a CNC-CNF-mixed film.

In order to characterize the resulted films, transparency, thickness, and tensile strength of the resulting films were measured. Then, surface topography of the film and conductive layer were observed by both scanning probe microscopy (SPM) and focused ion beam-scanning electron microscopy (FIB-SEM). Furthermore, the electric conductivity was measured after annealing the oil-based conductive ink which was applied onto the film by inkjet printing.

4.3 Experimental

4.3.1 Sample preparation

Commercially available CNCs prepared by sulfuric acid hydrolysis (University of Maine, USA) was homogenized in water, then the suspension was casted in a petri dish to obtain a CNC film (C-film; C-series). For some samples, a mixture of TEMPO-oxidized wood pulp-based cellulose nanofibers (CNFs; TEMPO-CNFs 1% in weight ratio, Nippon paper industries co. ltd., Japan) and CNCs was applied to CF-film fabrication (CF-series). A 4% (in weight ratio) of CNC suspension was prepared by dissolving CNCs in distilled water. Dried C-films with different grammage (g/m^2) were prepared by adjusting the amount of CNC suspension, and dried CF-films were prepared by mixing CNC suspension with CNF slurry (Table 4). The grammage of CF-

films was controlled to be similar with “C-40”, which is around 70–80 g/m^2. After all, oil-based silver nanopaste (O-AgNPs ink; NPS-JL, Harima Chemicals Group, Inc., Japan) was introduced onto films by an inkjet printer (Dimatix DMP-2831, Fujifilm, Japan).

4.3.2 Characterization of films

Film thickness (Tozai seiki co. ltd., Japan) was measured from 10 positions each of three test specimens. Then, a zero-span (ZS) tensile tester (Pulmac inc., USA) was used for evaluating the mechanical property of films. The specimen for ZS tensile strength was cut into 2 cm ×8 cm to fit the pressure blade (Figure 23), and the ZS tensile load was obtained at a clamping pressure of 60 psi. The reading value was calibrated to failure load by following its manual. Then, failure load was divided by the width to obtain ZS tensile strength. After divided ZS tensile strength by grammage, ZS tensile index was calculated. Then, folding endurance was measured with a tester (Toyo Seiki Seisaku-sho Ltd., Japan) by folding the specimen left and right both at 135°at a certain speed with a 1 kg weight on the top of the plunger, and then the number of double-fold until it fractured was counted. Folding endurance was calculated by converting the number of double-folds (fold number) to the logarithm (to the base of ten).

Measurements above were conducted in a conditioning room at 20°C and 50% in relative humidity (RH). Wettability of the films was studied by collecting the contact angle of a 0.5 μL water-drop on the films each 100 ms in 6000 ms (6 seconds) by a contact angle meter (DMs-401, Kyowa Interface Science Co., Ltd., Japan).

4.3.3 Structure of films and oil-based conductive tracks

O-AgNPs ink was introduced onto films by an inkjet printer (Dimatix DMP-2831, Fujifilm, Japan) and the resistance was measured after annealing at 110°C for 45 minutes. The surface structure was observed by field emission scanning electron microscopy (FE-SEM; SU-8020, Hitachi-hightech, Japan) and a FIB-SEM (600i,

Helios NanoLab, USA). Owing to FIB-SEM, the cross section was made by an ion beam (the place circled by dash-line in Figure 24-a, b); thus, the thickness of O-AgNP layer as well as the interface between O-AgNPs and film were observed. Then, SPM (E-sweep, Hitachi High-Tech Science, Japan) was used for the topographical observation with a dynamic force mode (DFM) and a cantilever “SI-DF20” with a tip radius smaller than 10 nm.

Table 4 List of C-films and CF-films.

Sample name	CNC: CNF (in mass.)	Thickness (mm)
C-20	100:0	0.02
C-40	100:0	0.04
C-60	100:0	0.08
C-80	100:0	0.10
CF-9-40	90:10	0.05
CF-8-40	80:20	0.05
CF-7-40	70:30	0.05
CF-6-40	60:40	0.06
CF-5-40	50:50	0.05
CF-4-40	40:60	0.05
CF-3-40	30:70	0.05
CF-2-40	20:80	0.05
CF-1-40	10:90	0.05
CF-0-40	0:100	0.05

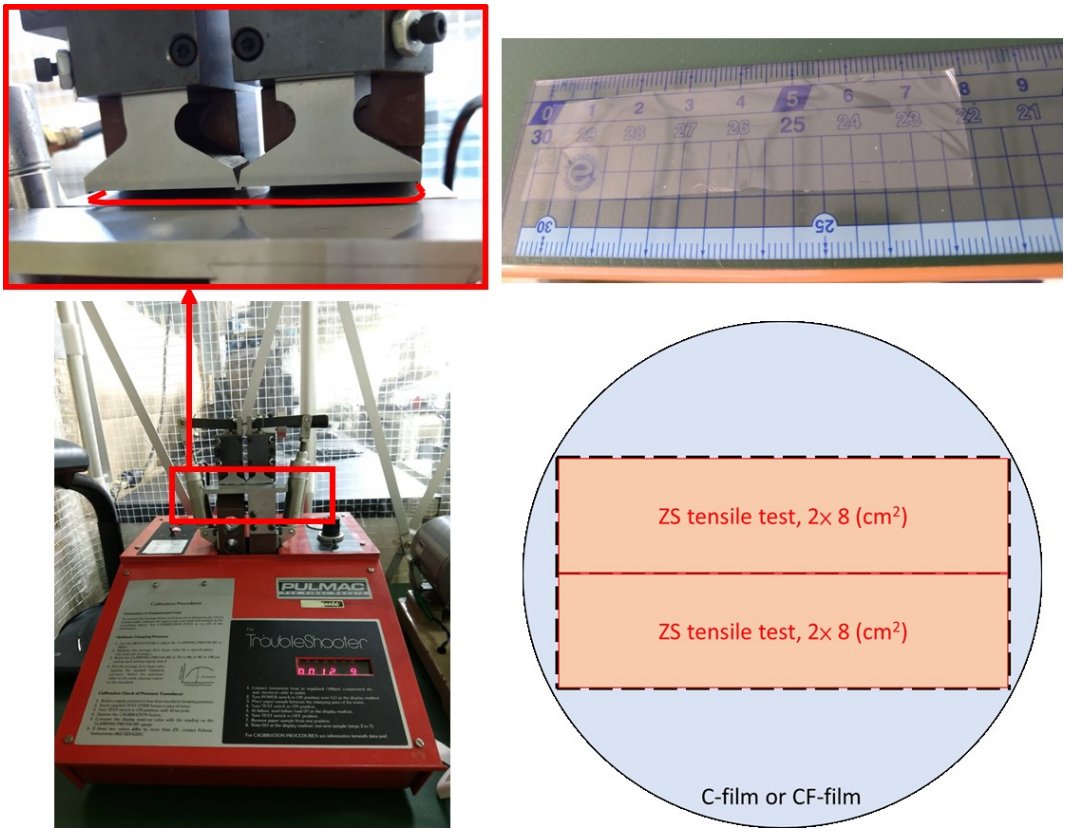

Figure 23 ZS tensile strength measurement.

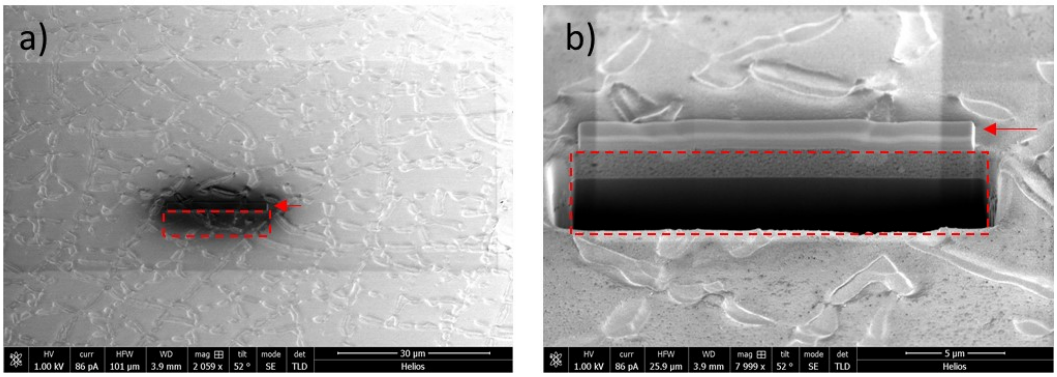

Figure 24 Observation of cross section by FIB-SEM. First, a brick of platinum was coated, as the arrows point in (a) and (b), in front of an ideal place where circled by the broken line in (a). Then, the hole as (b) was dug by an ion beam.

4.4 Result and discussion

4.4.1 Characterization of films

C-film and CF-film casts were successfully fabricated by drying at 50°C until the weight became almost 0 (Figure 25). A chiral nematic texture was observed at the cross section of a C-film (Figure 26) by SEM. As reported in references, this structure suggested that with a slow evaporation of solvent, chiral nematic self-assembly happened to form such a helical structure [1, 6]. Also, the films were observed by setting them between cross polarizers. Light passed through cross polarizers with a film between them because of the supposed chiral nematic ordering of CNCs (Figure 27-a). Because of different refractive indices for polarization along and perpendicular to CNC particles, a birefringent pattern was observed in each film (Figure 27-b, d). CNFs were also reported to dispersed in alignment through surface carboxylation like TEMPO-oxidization [7]; however, it was found to be darker as shown in Figure 27-c and d, suggesting the alignment of CNFs is limited. With a CNC composition less than 60%, CF-films were not suggested to exhibit specific ordering and thus the light didn't pass-through two polarizers (Figure 28). Fibers with relatively large aspect ratio was pointed out to result in the limitation of CNF alignment. [2]

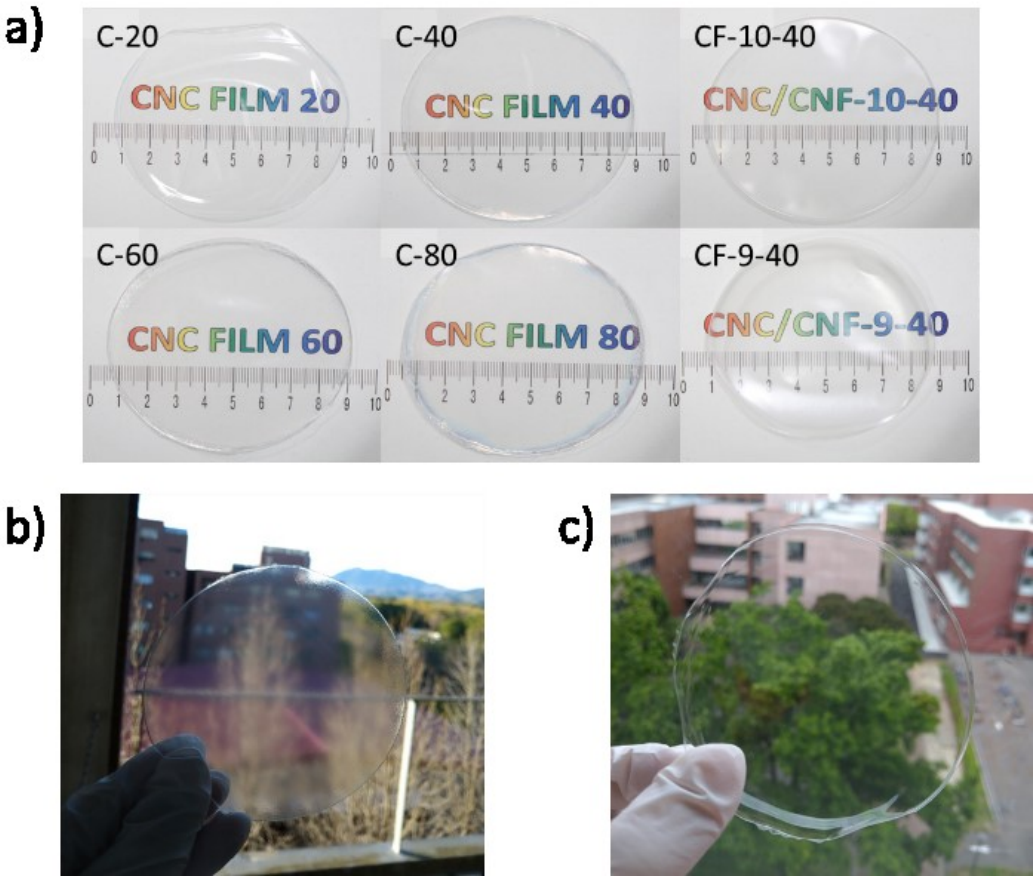

Figure 25 Fabricated C-films and CF-films. (b): Transparent C-film (Take “C-40” as example). (c): Transparent CF-film (Take “CF3-40” as example).

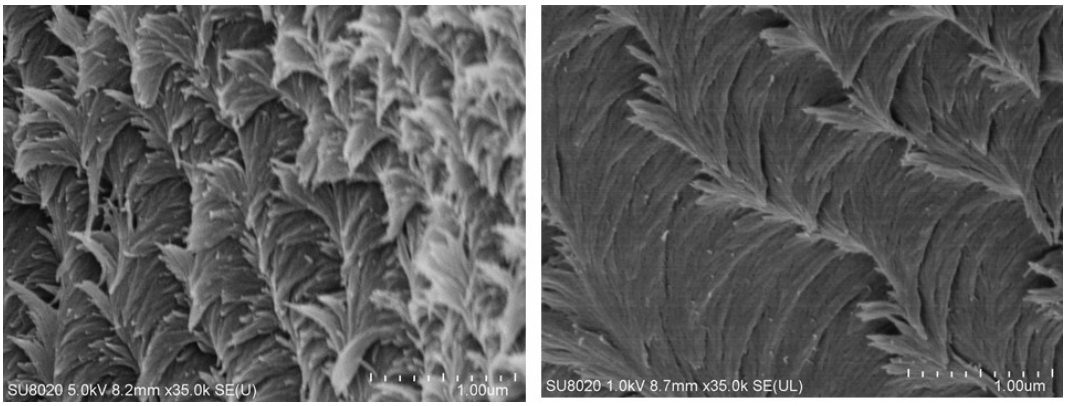

Figure 26 Cross section view of a C-film.

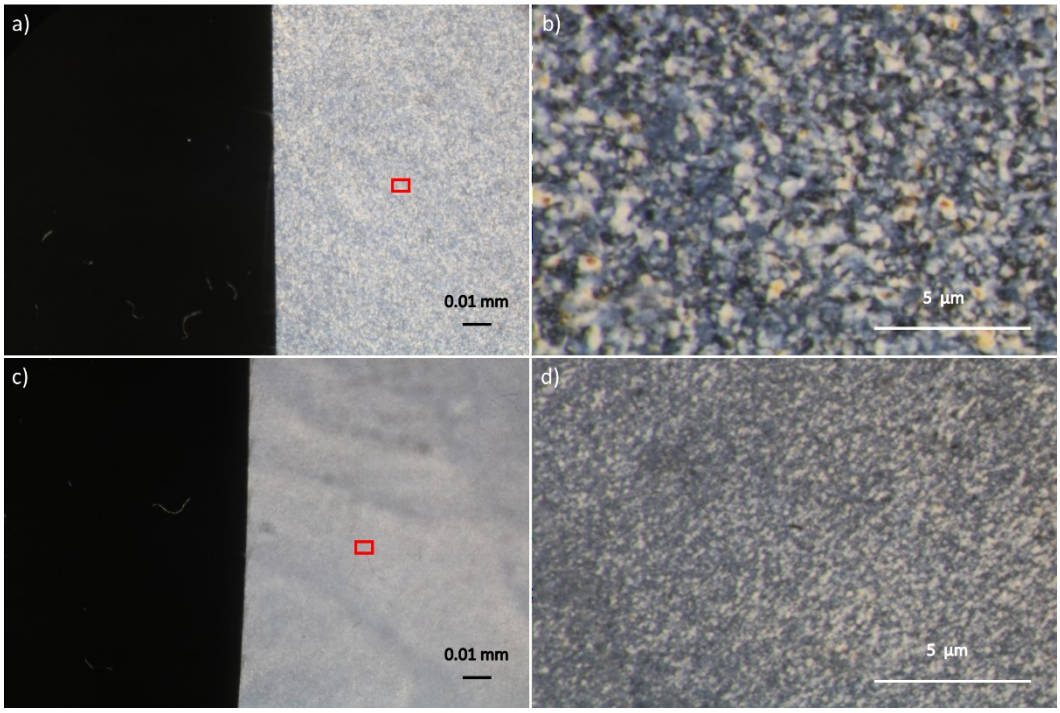

Figure 27 A C-film (a, b) and CF-film (c, d) were put between cross polarizers. In (a) and (c), the left side is the place without films inside but “C-40” and “CF9-40” was put in the right side of (a) and (c) respectively. Then, (b) and (d) are close-ups of the red rectangles in (a) and (c), respectively.

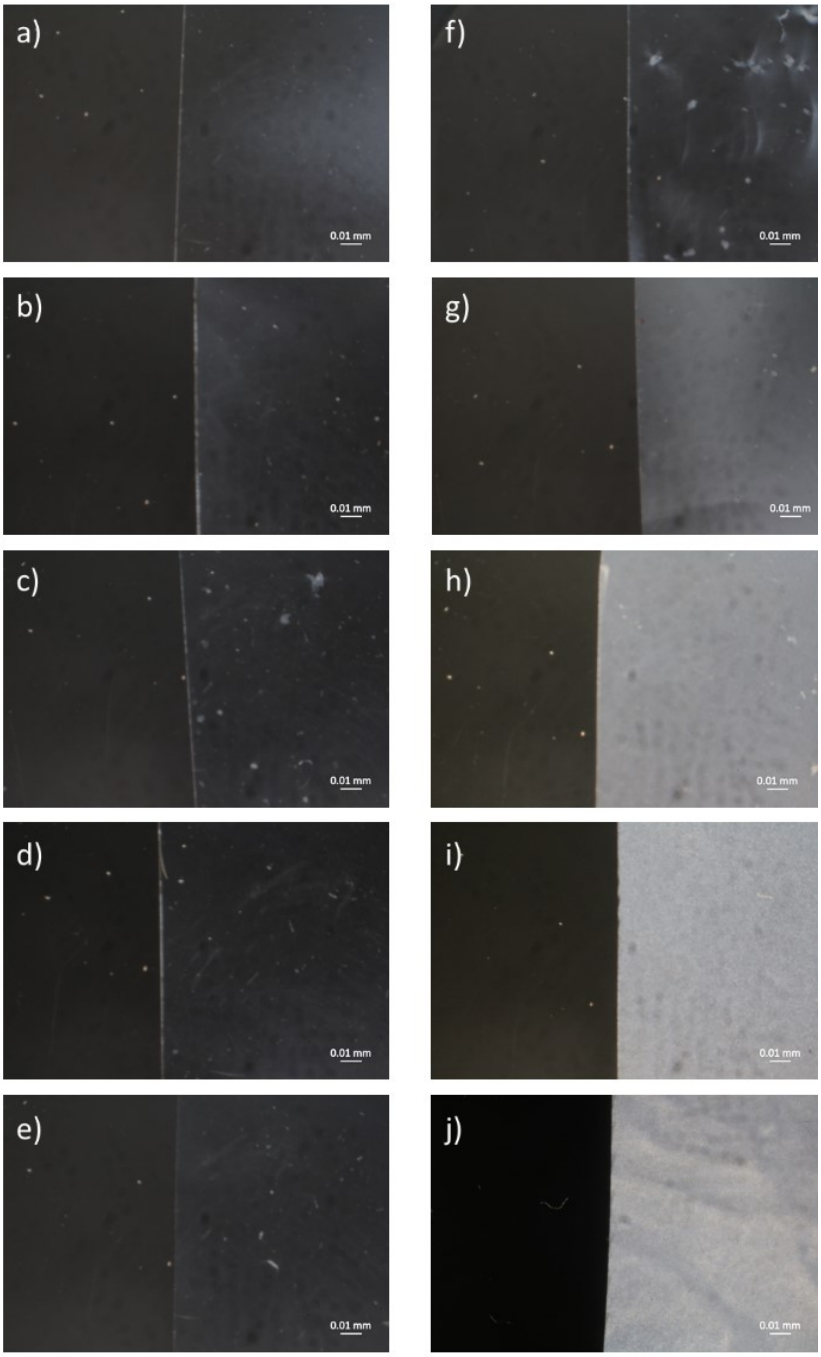

Figure 28 CF-films were put between cross polarizers: from (a) to (j) are CF-0-40, CF-1-40, CF-2-40, CF-3-40, CF-4-40, CF-5-40, CF-6-40, CF-7-40, CF-8-40, CF-9-40. The left side in each photo is the place without films inside.

4.4.2 Mechanical property and wettability of films

Tensile strength was calculated from the ZS tensile load divided by the grammage. A higher the value is, a relatively stronger ZS tensile load it can bare in a same unit of area. Based Figure 29-a, a decreasing of tensile strength was observed with an increased grammage of a C-film. However, with an addition of CNFs (Figure 29-b) but keeping the grammage as same as “C-40”, tensile strength was improved, suggesting that CNFs reinforce the film while the grammage kept low. On the other hand, the folding endurance of CF-films was also improved with CNF addition. It showed a positive correlation between the CNF ratio and folding endurance (Figure 30). In the case of a pure CNF film (CF-0-40), a folding number as high as 777 times was measured. Then, there was no significant difference of contact angle between samples when taking a look at the averaged contact angle within 6 sec. Each of them showed a contact angle above 40° but lower than 90°, suggesting a hydrophilic surface.

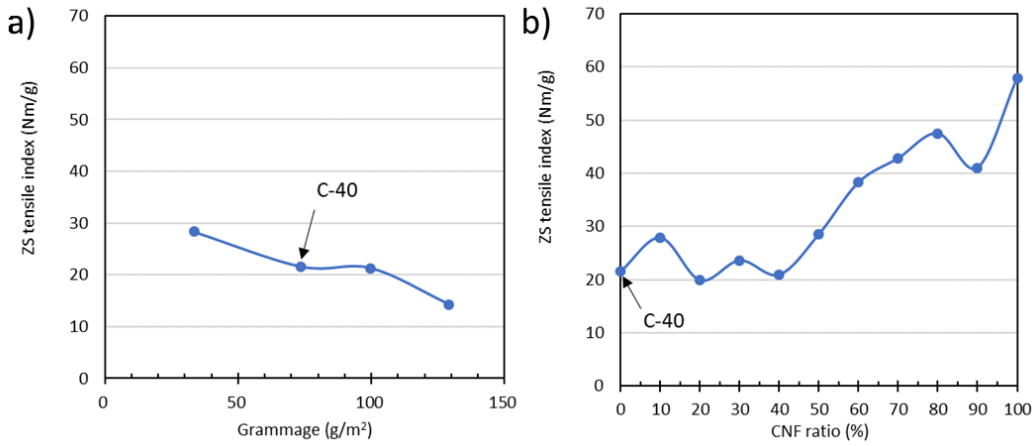

Figure 29 (a): ZS tensile strength and grammage of films. (b): ZS tensile strength and CNF ratio of films.

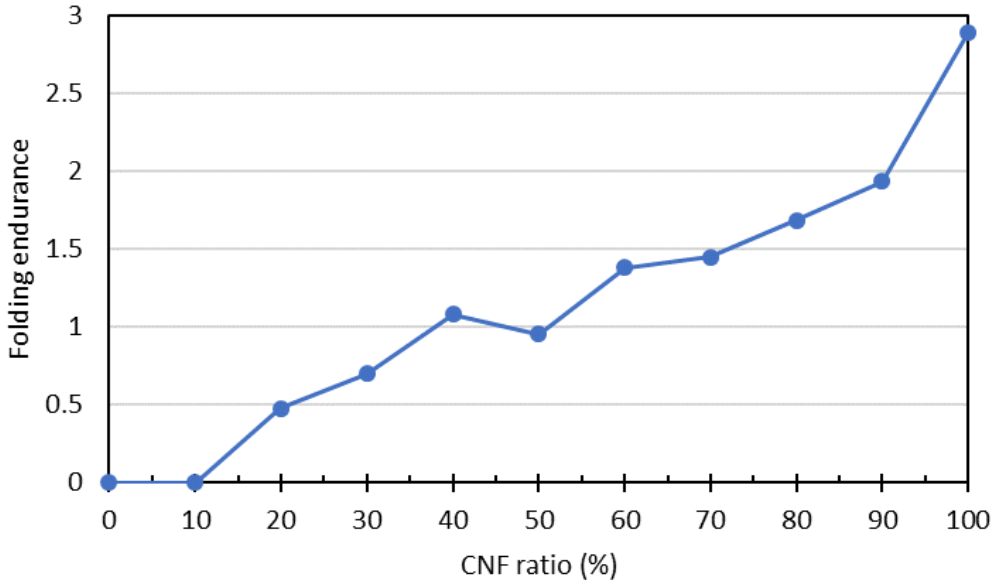

Figure 30 Folding endurance and CNF ratio.

4.4.3 Topographical observation of films and O-AgNP areas

A 1 μm square of film surfaces was scanned and observed by SPM. Spindle-like CNC cylinders were found to arrange randomly on the surface, which might be regarded as the isotropic phase formed on the top while the phase separation occurred during drying (Figure 31-a). CNF were found to entangle with each other (Figure 31-b).

Then, the O-AgNP area showed a parched earth on films both under SPM observation (Figure 32-a) and FIB-SEM (Figure 32-b). Fortunately, the layer of O-AgNPs was not destroyed due to the parch-earth-structure resulted by drying. A2-μm-thick O-AgNP layer was introduced on films by inkjet printing. A clear interface between an O-AgNP layer and a surface of film, pointed out by arrows in Figure 33, was observed in each sample. “C-40”, a film without the addition of CNF, showed an O-AgNP layer of 1.420 μm in averaged. As to a CF-film, with a higher proportion of CNCs, a thinner O-AgNP layer was noticed: “CF10-40” showed an O-AgNP layer of 1.276 μm, whereas the layer on “CF9-40” was 2.118 μm, in averaged.

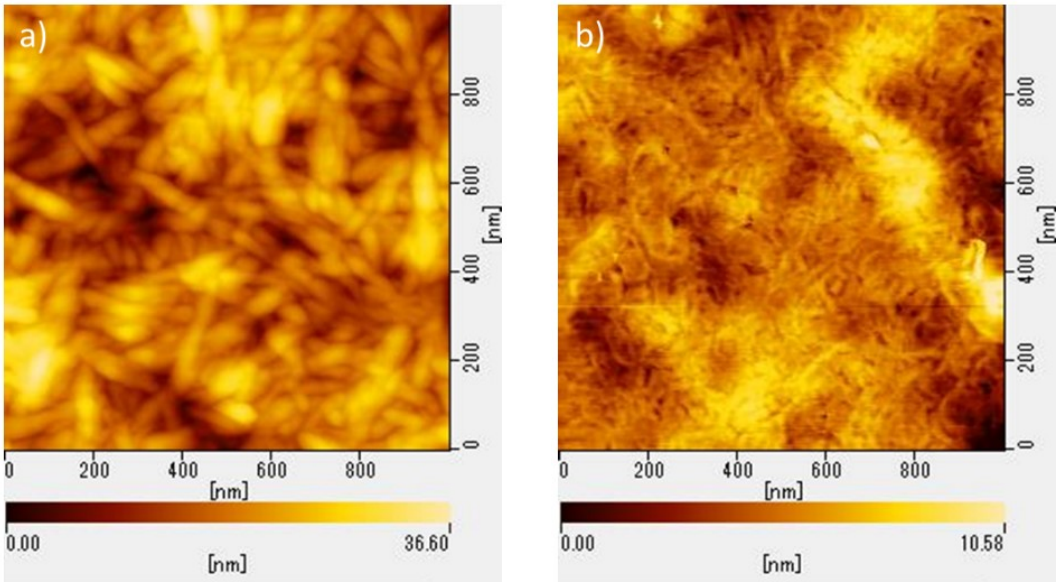

Figure 31 (a): Surface of a C-film ("C-40" as an example). (b): Surface of "CF-0-40".

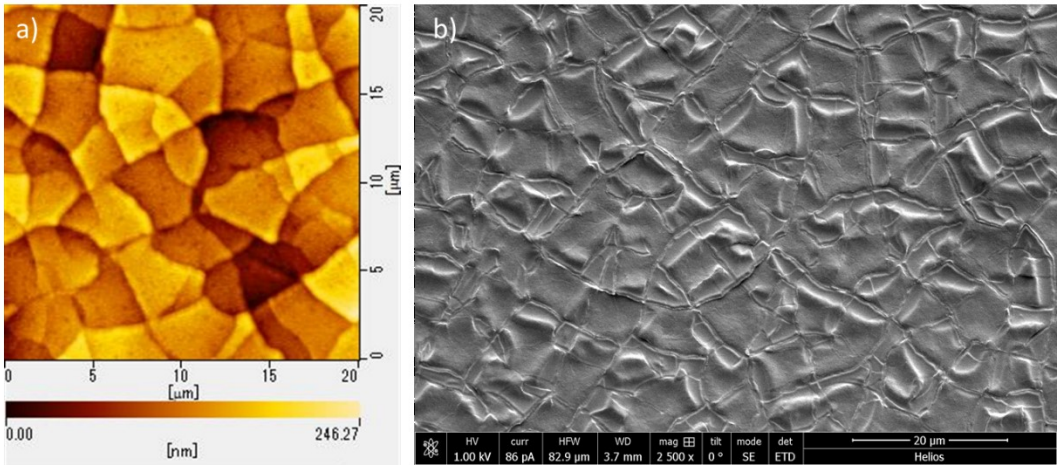

Figure 32 Ground of O-AgNPs on a film (“C-40” as an example).

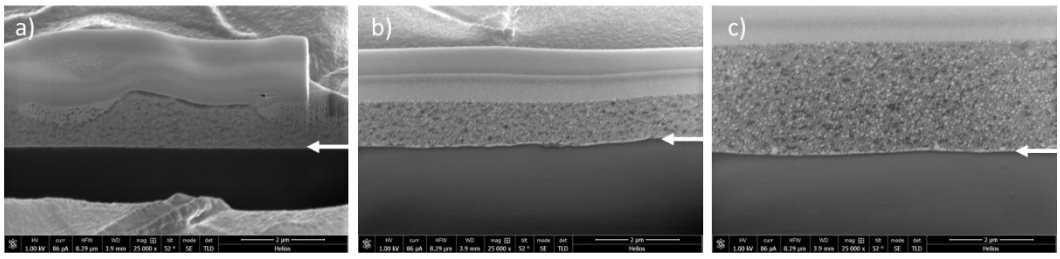

Figure 33 Thickness of an O-AgNP layer on (a) “C-40”, (b) “CF10-40”, and (c) “CF9-40”.

4.4.4 Electrical performance of O-AgNP tracks

Circuit was prepared by putting pieces of copper tape on the designed location of a film. Copper tape was used at the conjunction place with resistance, light-emitting diode (LED,) and batteries. Then O-AgNPs ink was printed onto the film with some overlaps between the ink and copper tape and then annealed as the way explained in 4.3.3. After annealing, crocodile clips were used to connect the printed tracks with resistance, LED, and batteries (Figure 34). All the C-films and a CF-film, CF-9-40, was tried. All of them showed a resistance of 0 Ω, thus suggesting an optimal potential to be used as electric circuits in display, antenna, etc.

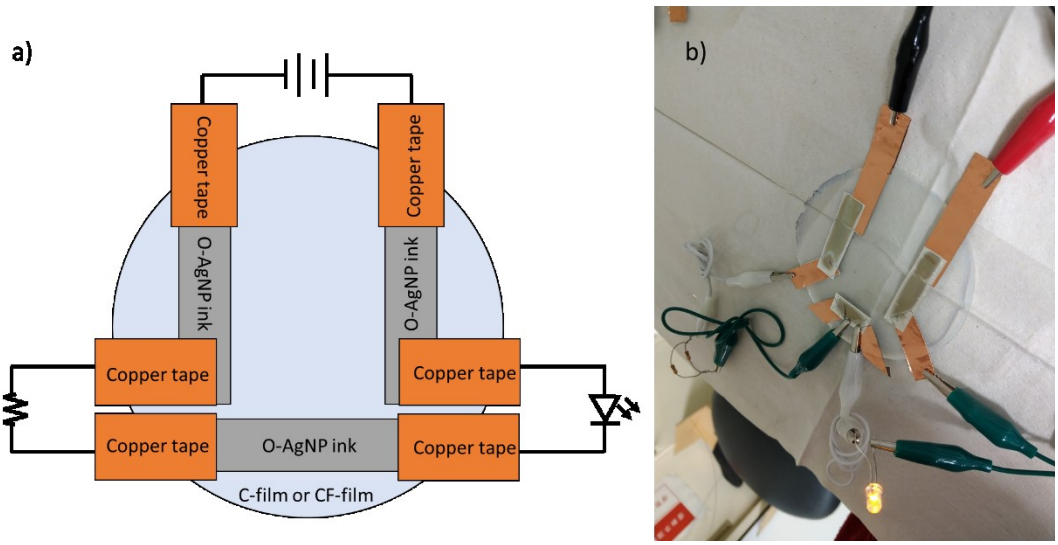

Figure 34 Design of the circuit on a film.

4.5 Conclusion

Thin transparent C-film and CF-film were fabricated by casting CNC/CNF suspension on a petri dish. CNF reinforced C-film to bear a higher tensile load and exhibit a higher folding endurance. Both chiral nematic ordering and helical structure were observed in a C-film and a CF-film with more than 60% of CNCs. O-AgNPs showed a parched earth on both C-film and CF-film. The O-AgNP layer was thicker on a CF-film than a C-film. Resistance of O-AgNP tracks on C-film and CF-film were low enough to be applied as a circuit.

Reference

1 Lagerwall, J.P.F.; Schütz, C.; Salajkova, M.; Noh, J-H.; Park, J.H.; Scalia, G.; Bergström L. Cellulose nanocrystal-based materials: from liquid crystal self-assembly and glass formation to multifunctional thin films. *NPG Asia Mater* **2014**, *6*, e80. https://doi.org/10.1038/am.2013.69

2 Salas, C.; Nypelö, T.; Rodriguez-Abreu, C.; Carrillo, C.; Rojas, O.J. Nanocellulose properties and applications in colloids and interfaces. *Current Opinion in Colloid & Interface Science* **2014**, *19* (5), 383–396.

3 Araki, J.; Kuga, S. Effect of trace electrolyte on liquid crystal type of cellulose microcrystals. *Langmuir* **2001**, *17*, 4493–4496.

4 Pan, J.; Hamad, W.; Straus S.K. Parameters affecting the chiral nematic phase of nanocrystalline cellulose films. *Macromolecules* **2010**, *43* (8), 3851–3858.

5 Roman, M.; Winter, W.T. Effect of sulfate groups from sulfuric acid hydrolysis on the thermal degradation behavior of bacterial cellulose. *Biomacromolecules* **2004**, *5*, 1671–1677.

6 Zhang, Y.P.; Chodavarapu, V.P.; Kirk, A.G.; Andrews, M.P. Structured color humidity indicator from reversible pitch tuning in self-assembled nanocrystalline cellulose films. *Sensors and Actuators B: Chemical* **2013**, *176*, 692–697.

7 Saito, T.; Uematsu, T.; Kimura, S.; Enomae, T.; Isogai, A. Self-aligned integration of native cellulose nanofibrils towards producing diverse bulk materials. *Soft Matter* **2011**, *7*, 8804–8809.

Chapter 5

Overall Conclusion

Inkjet-printed electronic devices with a cellulose-based substrate were reviewed, and the problem caused by complex surface environment of paper was noticed. Thus, cellulose nanocrystals (CNCs), a nano-scale cellulosic material with a high crystallinity and unique optical properties was focused in this study.

Dry hardwood pulps were used to prepare CNCs with a variety of hydrolysis conditions. A high hydrolysis temperature (65 °C) or stronger sulfuric acid concentration (63%) was preferred to produce redispersible CNCs with successfully grafted sulfate groups. Then, negative surface potential was observed for CNC particles owing to sulfate groups introduced via hydrolysis. Moreover, at a high electrolyte concentration, CNCs had a thin double layer, and thus the end effect was not very significant during electrophoresis. Instead, at lower electrolyte concentrations (< 25 mM), the double layer remained relatively thick, suggesting the Ohshima-Overbeek averaged equation and the Ohshima-Overbeek perpendicular equation explain the experimental data more accurately than Smoluchowski's equation. With the consideration of cylindrical shape and the end effect, which became remarkable in the case of a short cylinder with a remarkable surface charge, a new method based on the Ohshima-Overbeek (length) equation that has never been applied to CNCs before was suggested.

Then, water-based CNC suspensions were suggested as a pretreatment material of photo-grade inkjet paper, improving a linkage between paper and water-based silver nanoparticles ink (W-AgNPs ink). An enhanced wetting surface of W-AgNPs ink was suggested with pre-printed CNCs. Also, a facilitated W-AgNPs ink penetration and

resulted firm and robust tracks were developed with CNCs. Hence, an achievement on a better conductive performance of paper-based conductive area was reached owing to a CNC undercoat.

Considering a wider application of a transparent conductive device, and an optimal conductivity brought by metallic inks which form interconnected phase after annealing, CNCs won the admiration to fabricate transparent and heat resistant casting films. Transparent films with unique optical properties thanks to the chiral nematic ordering and helical structure were prepared with a proportion of CNC higher than 60%. Each film was suggested as the substrate of O-AgNPs. The O-AgNP layer was thicker on a CNF-auditioned film than a pure CNC film though, O-AgNP tracks on both were low enough to be applied as a circuit.